

A direct controlled-phase gate between microwave photons

Adrian Copetudo,¹ Amon M. Kasper,¹ Tanjung Krisnanda,¹ Gregoire Veyrac,¹ Shushen Qin,¹ Hui Khoon Ng,^{2,1} and Yvonne Y. Gao^{1,2,*}

¹*Centre for Quantum Technologies, National University of Singapore, Singapore*

²*Department of Physics, National University of Singapore, Singapore*

(Dated: March 17, 2026)

Useful quantum information processing ultimately requires operations over large Hilbert spaces, where logical information can be encoded efficiently and protected against noise. Harmonic oscillators naturally provide access to such high-dimensional spaces and enable hardware-efficient, error-correctable bosonic encodings. However, direct entangling operations between oscillators remains an outstanding challenge. Existing strategies typically rely on parametrically activating interactions that populate the excited states of an ancillary nonlinear element. This induces an effective interaction between the oscillators, at the expense of introducing additional dissipation channels and potential leakage from the encoded manifold. Here, we engineer a Raman-assisted cross-Kerr interaction between microwave photons hosted in two superconducting cavities, without exciting the nonlinear element, thereby suppressing coupler-induced decoherence. This approach generates a direct coupling between microwave photons that is exploited to implement a controlled-phase gate within the single- and two-photon subspaces of two oscillators, directly entangling them. Finally, we harness this dynamics to map the photon-number parity of a storage cavity onto an auxiliary oscillator rather than a nonlinear element, enabling error detection while protecting the storage mode from measurement-induced decoherence. Our work expands the bosonic circuit quantum electrodynamics (cQED) toolbox by enabling coherence-preserving direct photon-photon interactions between oscillators. This realizes an entangling gate that operates entirely within a bosonic code space while suppressing decoherence from nonlinear ancilla excitations, providing a key primitive for fault-tolerant bosonic quantum computing.

Quantum harmonic oscillators—whether manifested as flying photons, stationary electromagnetic modes or phononic excitations of motion—represent one of the most attractive platforms for quantum information processing. Their naturally weak environmental coupling yields exceptionally long coherence times and enables low-loss propagation over macroscopic distances, making them a native choice for quantum key distribution [1–3] and quantum networks [4, 5]. Moreover, the large Hilbert space accessible within a single oscillator mode allows for hardware-efficient encoding of quantum information, a feature that has enabled recent demonstrations of quantum error correction (QEC) beyond the break-even point in several physical platforms [6–13]. These intrinsic advantages have driven landmark achievements across quantum communication [14–16], metrology [17, 18], and computation [19, 20], establishing bosonic systems as efficient carriers of quantum information and valuable building blocks for robust quantum computation.

However, the central challenge in harnessing bosonic modes for quantum computation is the difficulty of creating direct photon-photon interactions [21] - a key ingredient for deterministic entanglement and universal gate operations. Two harmonic oscillators in close proximity to one another naturally hybridize into linear normal modes that remain non-interacting. Consequently, deterministic entanglement is typically implemented using parametrically driven dynamics mediated by excitations in a non-

linear ancillary element [22–25]. In existing bosonic circuit quantum electrodynamics (cQED) demonstrations, for instance, each harmonic mode is entangled with the excited states of a nonlinear coupler to engineer an effective interaction between the oscillators [26–29]. Although successful, such schemes necessarily lead to leakage outside the protected bosonic code space and open additional decoherence channels for the oscillators, limiting their gate fidelity and fault-tolerance [30–32].

In this work, we implement a direct Raman-assisted cross-Kerr interaction between microwave photons hosted in two superconducting cavities. This engineered coupling, which can be activated on-demand, is two orders of magnitude stronger than the residual always-on cross-Kerr. We use this nonlinear dynamics to perform a controlled-phase gate in the single- and two-photon subspace, with average fidelities above 95%. Importantly, our technique generates entanglement directly between the two oscillator fields without ever populating the excited states of the nonlinear coupler, while preserving the photon number in both cavities. This mitigates the coupler-induced decoherence and ensures that the system remains within the encoded subspace throughout the entangling operation, making our method inherently compatible with a wide range of existing bosonic QEC methods. Further, we leverage this cross-Kerr to perform a bosonic parity check on a storage cavity encoded in a biased-erasure [33, 34]. Heralded by the state of the ancillary cavity, the storage lifetime is enhanced without any interactions with auxiliary nonlinear elements. Our direct photon-photon interaction provides a valu-

* Corresponding author: yvonne.gao@nus.edu.sg

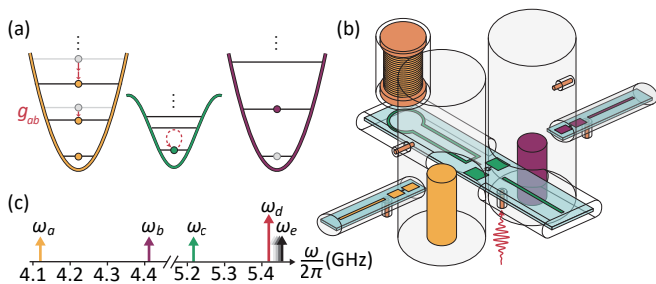


FIG. 1. **Driven cross-Kerr protocol and experimental device.** (a) Conceptual illustration of the engineered direct cross-Kerr, g_{ab} , between two harmonic oscillators mediated by a nonlinear coupler, where a photon in one mode shifts the energy levels of the other without physically populating the coupler. (b) Schematic of the experimental device, consisting of two 3D superconducting cavities, each coupled to its own side transmon used for state preparation and tomography. A central asymmetric SQUID acts as the coupler and is flux-biased by a superconducting coil via pick-up loop transformer. (c) Frequency arrangement used in this work. A strong pump is placed at ω_d with a detuning $\Delta/2\pi$ of few MHz from the resonance exchange $|1\rangle|0\rangle|g\rangle \leftrightarrow |0\rangle|1\rangle|e\rangle$ occurring at $\omega_e = 5.20$ GHz. Higher photon resonances are shifted down in frequency by multiples of χ_a and χ_b .

able tool for fault-tolerant information processing using error-correctable bosonic modes [35].

Generally, the cross-Kerr interaction between two oscillators, Alice and Bob, takes the form

$$\hat{H}_\chi/\hbar = g_{ab} \hat{a}^\dagger \hat{a} \hat{b}^\dagger \hat{b}, \quad (1)$$

where a and b are the annihilation operators of the two cavity modes, and g_{ab} denotes the cross-Kerr coupling strength. Intuitively, this is a direct nonlinear coupling between two bosonic elements where the resonance frequency of one depends on the photon population of the other, as illustrated in Fig. 1(a).

In the context of bosonic cQED systems, the oscillators are typically realized using high-Q aluminum superconducting stub cavities, as shown in Fig. 1(b). Here, Alice and Bob, with frequencies $\omega_a/2\pi = 4.12$ GHz and $\omega_b/2\pi = 4.41$ GHz, are dispersively coupled to a common nonlinear coupler in the form of an asymmetric SQUID, with strength χ_a and χ_b , respectively. The coupler frequency, $\omega_c/2\pi$, can be tuned from 4.3 GHz to 5.7 GHz by a DC flux applied via a superconducting transformer loop [36, 37] from a distant coil, which preserves cavity coherences with single photon lifetimes exceeding 0.8 ms in both Alice and Bob. In this architecture, H_χ arises natively due to the mixing of the two oscillator bosonic fields mediated by the nonlinear coupler, whose dynamics is akin to a third-order $\chi^{(3)}$ nonlinear medium. However, this always-on interaction is generally undesirable and carefully minimized.

To achieve a strong on-demand cross-Kerr without populating the nonlinear coupler, we off-resonantly drive a coherent exchange interaction between the states

$|1\rangle_a|0\rangle_b|g\rangle_c$ and $|0\rangle_a|1\rangle_b|e\rangle_c$ to activate the dynamics given by

$$\hat{H}_d/\hbar = g_1 \left(e^{i\Delta t} \hat{a}^\dagger \hat{b} |g\rangle\langle e| + \text{h.c.} \right), \quad (2)$$

where $|g\rangle$ ($|e\rangle$) denote the ground (excited) state of the coupler, g_1 the exchange rate, and Δ the detuning between the drive frequency, ω_d , and the resonant exchange frequency, $\omega_e = \omega_c + \omega_b - \omega_a - \chi_b$.

In the Raman regime, where the drive is far detuned from resonance by $\Delta \gg g_1$, the near-resonant interaction terms of Eq. 2 oscillate rapidly and are eliminated under the rotating-wave approximation. The dynamics are thus governed by second-order processes in which the state $|1\rangle|0\rangle|g\rangle$ only virtually transitions through $|0\rangle|1\rangle|e\rangle$. We treat this off-resonant interaction perturbatively via a Schrieffer–Wolff transformation [38, 39] to derive the effective cross-Kerr Hamiltonian,

$$\hat{H}_{\text{eff}}/\hbar = g_{ab} \hat{a}^\dagger \hat{a} \hat{b}^\dagger \hat{b} |g\rangle\langle g|, \quad (3)$$

where the strength of the engineered coupling is given by

$$g_{ab} \approx \frac{g_1^2}{\Delta} \frac{\Delta - \chi_b}{\Delta + \chi_b}. \quad (4)$$

We experimentally calibrate g_1 by loading a photon in Alice and driving the coupler at a frequency ω_e . This activates the coherence exchange that leads to oscillations of the cavity populations as a function of the drive duration. An exemplary measurement is shown in Fig. 2(a). This time dynamics is consistent with a full master equation simulation with system decoherence taken into account [39]. The exchange rate extracted from the period of this oscillation, $g_1/2\pi = 1.024 \pm 0.004$ MHz, is in good agreement with the analytically predicted value of $g_1/2\pi \approx \sqrt{\chi_a \chi_b} \xi/2\pi \approx 1.01$ MHz, where we used the independently measured dispersive shifts $\chi_a/2\pi \approx 2.8$ MHz and $\chi_b/2\pi \approx 3.0$ MHz, and an effective drive strength $|\xi| \approx 0.35$, obtained from coupler AC Stark shift measurements [39].

Achieving a high-quality entangling operation via this dynamics requires maximizing the on-off ratio while minimizing coupler excitation. The former is achieved by optimizing the frequency configuration of the coupler to suppress the native always-on cross-Kerr interaction, K_{ab} , between Alice and Bob, while still allowing a sizable g_1 [39]. Balancing these considerations, we bias the coupler at a frequency of $\omega_c/2\pi = 5.22$ GHz for the rest this work, where we can realize an exchange rate up to $g_1/2\pi = 0.8$ MHz with a weak static cross-Kerr of $K_{ab}/2\pi \approx 0.3$ kHz.

Next, we consider the trade-off between the residual coupler excitations and the gate speed. We calibrate g_{ab} at different detunings Δ with a Ramsey experiment where we compare the phase accumulated by Alice when Bob is either in $|0\rangle$ or $|1\rangle$. The experimentally extracted cross-Kerr strength is shown in Fig. 2(b) at both positive and negative detunings. We observe that, in agreement with Eq. 3, that $|g_{ab}|/2\pi$ increases from ~ 10 kHz

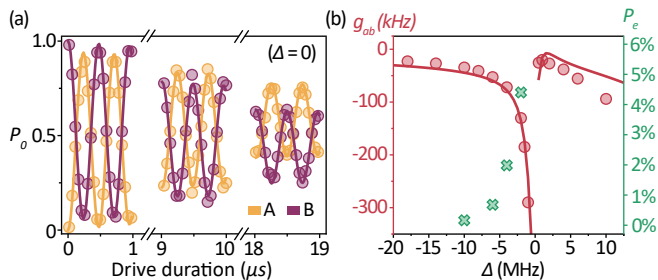


FIG. 2. **Calibration of the cross-Kerr protocol parameters.** (a) Coherent exchange of population between $|10g\rangle$ and $|01e\rangle$ modes when $\Delta = 0$ obtained by monitoring the vacuum population of Alice (yellow) and Bob (purple). Oscillation frequency corresponds to $g_1/2\pi = 1.024 \pm 0.004$ MHz. The data (circles) agrees well with master equation simulations (lines) with the independently measured cavity and coupler decoherence. (b) Strength of engineered cross-Kerr (red), extracted from cavity Ramsey experiments, and residual coupler excitations (green) as a function of Δ . Solid line is a Floquet simulation with experimentally extracted Hamiltonian parameters [39].

to ~ 300 kHz as Δ goes from -20 MHz to -2 MHz. It is interesting to note the asymmetry of the engineered cross-Kerr for $\Delta > 0$, due to the interplay between the drive detuning and the dispersive shift between the coupler and Bob [39].

Crucially, when $\Delta \sim g_1$, the oscillating terms of H_d are no longer eliminated by the RWA, as they oscillate slowly enough to contribute at first order, resulting in real excitations of the coupler mode. The upper bound of the coupler excitation, P_e^{\max} , is given by

$$P_e^{\max} = \frac{g_1^2}{g_1^2 + \Delta^2}. \quad (5)$$

We experimentally measure the average steady-state residual populations of the coupler after a $\sim 5 \mu\text{s}$ drive at different detunings, as shown in green markers in Fig. 2(b). Based on this, we choose an operating point with $\Delta = -6$ MHz, that yields a large on-off ratio of $g_{ab}/K_{ab} \gtrsim 250$ while ensuring minimal coupler excitations below $P_e < 1\%$.

We showcase the performance of our engineered cross-Kerr as a direct controlled-phase (CPHASE) operation for bosonic states in the $0/n$ subspace, which forms a biased-erasure encoding with logical codewords of the form $\{|0\rangle, |n\rangle\}$ (with $n \geq 1$). Concretely, the time evolution under Eq. 1 for a duration T yields a non-zero phase only to the state

$$|1\rangle_L |1\rangle_L = |n_a\rangle |n_b\rangle \rightarrow e^{-ig_{ab}n_a n_b T} |n_a\rangle |n_b\rangle = e^{i\phi} |1\rangle_L |1\rangle_L, \quad (6)$$

where $\phi = -g_{ab}n_a n_b T$ is a continuous controlled-phase that can be tuned by changing the interaction time. More broadly, for any rotationally-symmetric bosonic code [40], this interaction can impart a controlled- Z gate by tuning the interaction strength and time such that

$g_{ab}T = \frac{\pi}{NM}$, where N and M are the rotational symmetries of each cavity encoding. This condition ensures that only the logical $|1\rangle_L |1\rangle_L$ component acquires a full π phase, while all other logical basis states remain unchanged due to acquiring phases that are integer multiples of 2π .

As an example, we characterize the CPHASE gate within the $0/1$ photon subspace, often used to implement dual-rail qubits [41, 42], by preparing Alice and Bob in different basis states and activating the cross-Kerr interaction for a variable duration. Alice state, initialized as $|+\rangle = (|0\rangle + |1\rangle)/\sqrt{2}$, remains unchanged under this dynamics when Bob is in $|0\rangle$, but acquires a continuous phase when Bob is in $|1\rangle$. The accumulated phase on Alice, extracted from the reconstructed density matrices [39] after each evolution time, is shown in Fig. 3(a). A cosine fit (solid line) indicates a calibrated controlled- Z (CZ) gate time of approximately $5.2 \mu\text{s}$. Moreover, by simply choosing the gate duration, we realize an effective controlled- T ($\phi = \pi/4$) and controlled- S ($\phi = \pi/2$) gates, at times $T = 1.3 \mu\text{s}$ and $2.6 \mu\text{s}$, respectively. We present the measured Wigner functions at some selected gate times in Fig. 3(b).

Next, we apply the calibrated CZ gate to Alice and Bob, both prepared in superposition states, $|+\rangle|+\rangle$, and probe the resulting entanglement between the microwave photons. The reconstructed state, which is a Bell pair of the form $\frac{1}{2}(|0\rangle|0\rangle + |0\rangle|1\rangle + |1\rangle|0\rangle - |1\rangle|1\rangle)$, is shown in the Pauli-operator representation in Fig. 3(d). The solid bars show the experimentally reconstructed values, which generally follow the ideal expectation values (solid line) and are consistent with the outcomes of master-equation simulations (dotted lines). In addition, we also include the resulting states after 3 and 5 CZ operations. Notably, the IZ and ZI components grow steadily with the number of gates, indicating that the dominant form of imperfection in our gate is photon loss from Alice and Bob. The other spurious components are consistent with imperfections in the the initial state preparation and miscalibrations of the gate duration. The inset displays the measured single-cavity Wigner functions of the maximally entangled state after one CZ gate. Each reduced state exhibits no visible phase structure and closely resembles a maximally-mixed state, consistent with the loss of local coherence upon tracing out the other subsystem.

Finally, we analyze the gate quality on different basis states in the $0/1$ encoding by tracking the state fidelities after applying multiple CZ operation. From a linear fit to the fidelity decay, we extract an average infidelity per gate of 2.6% and 3%, when the control is in $|0\rangle$ or $|1\rangle$, respectively. The infidelity is dominated by cavity decoherence during the gate, which are pronounced due to drive-induced decay [43–45] and dressed dephasing [46, 47]. Our results are in good agreement with the outcome of full master equation simulations (shaded regions), where we simulate the evolution of the experimentally reconstructed initial state under the cross-Kerr dynamics that include driven cavity decoherences. The

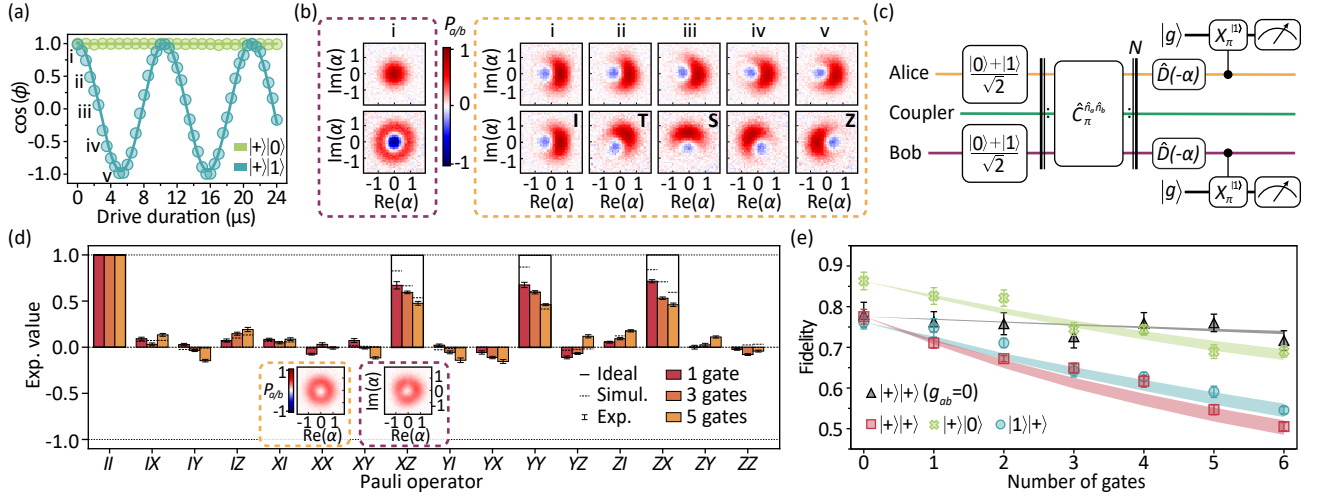


FIG. 3. **Controlled-phase gate in the single-photon manifold.** (a) Phase accumulated by Alice, initialized in $|+\rangle = (|0\rangle + |1\rangle)/\sqrt{2}$, as a function of the evolution time under H_{eff} , with Bob in state $|0\rangle$ (green) or $|1\rangle$ (turquoise). A full CZ gate is implemented in $5.244 \pm 0.008 \mu\text{s}$. (b) Sampled Wigner functions of Alice (yellow) and Bob (purple) at specific times corresponding to a controlled-S, T and Z gates. (c) Protocol used to obtain a maximally-entangled state, where cavities are prepared in $|+\rangle|+\rangle$. The CZ gates, $C_{\pi}^{n_a n_b}$, are applied N -times, followed by state tomography by sampling the populations of the oscillators in $|1\rangle$ after at optimized displacement points, α , in phase space [39]. (d) Pauli basis representation of the reconstructed two-cavity state after applying $N = 1, 3, 5$ gates to $|+\rangle|+\rangle$. Inset shows the Wigner functions of the statistical mixture in the oscillators when they are measured independently after one CZ gate. (e) Repeated application of C_{π} across a set of initial states. Dots are raw experimental data without any scaling. First points indicate that fidelity is limited by state preparation and measurement fidelity. Control experiment (black triangles) creates $|+\rangle|+\rangle$ without drive, has a infidelity of $0.7 \pm 0.3\%$ per gate. When the gate is activated, $|+\rangle|+\rangle$ (red squares) introduces an infidelity of $4.6 \pm 0.3\%$ per gate. Similarly, states $|+\rangle|0\rangle$ (green crosses) and $|1\rangle|+\rangle$ (blue circles) suffer an infidelity of $3.1 \pm 0.3\%$ and $3.7 \pm 0.2\%$ per gate, respectively. Shaded regions represent master equation simulations of dynamics given by Eq. 3. Spread corresponds to $\pm 10\%$ variation of cavity coherences observed in experiments.

width of the shaded bands corresponds to a $\pm 10\%$ variation in the coherence parameters, reflecting the typical day-to-day fluctuations observed in the system. We quantified the limitation due to the natural cavity decoherence by preparing the state $|+\rangle|+\rangle$ and reconstructing it after an idle time equivalent to the duration of several CZ gates (black line). The resulting infidelity, 0.5% per gate, matches the expected value based on the bare lifetimes and the gate duration.

To demonstrate the compatibility with multi-photon encodings, we apply the engineered cross-Kerr interaction to the biased-erasure encoding in the $0/2$ subspace. This offers two key advantages: first, the effective coupling strength increases due to the bosonic enhancement; second, standard photon-number parity checks via auxiliary transmons can be interleaved during and after the operation to detect and correct for errors, partially mitigating the drive-induced decay.

In this subspace, we increase the detuning to $\Delta/2\pi = -10 \text{ MHz}$ to account for the broader effective linewidth of the driven resonance and ensure that the residual coupler excitations are still suppressed. With this setting, we demonstrate a continuous CPHASE gate on the state $\frac{|0\rangle+|2\rangle}{\sqrt{2}}$ encoded in Alice with Bob in $|2\rangle$, indicating a CZ time of $1.94 \mu\text{s}$, see Fig. 4(a). Again, we extract quality of the operation by monitoring the infidelity

of the reconstructed states after repeated gate application. This yields an infidelity of $3.9 \pm 0.5\%$ per gate (turquoise line in Fig. 4(b)). By performing a standard parity measurement using the side auxiliary transmons at the end of the protocol and post-selecting on runs in which both cavities remain in an even-parity superposition, the extracted infidelity rate is reduced to $2.0 \pm 0.6\%$ per gate (green line). For comparison, the red line corresponds to the case where the control is prepared in $|0\rangle$. In this case, we apply the same gate drive and post-select on even parity, obtaining an infidelity of $0.9 \pm 0.3\%$ per gate. The difference between the two slopes is consistent with the expected increase in decoherence when the control cavity is populated with two photons rather than zero.

Although the standard parity check using auxiliary transmons is an effective means of suppressing imperfections arising from photon loss, it necessarily entangles the microwave photons with the transmons during the process and results in excursions out of the protected bosonic code space. To fully capitalize on the advantages of bosonic QEC, it would be desirable to perform parity checks on the encoded state using purely bosonic interactions. Our engineered cross-Kerr dynamics provides the key ingredient to accomplish this goal.

In the protocol described in Fig. 4(c), we encode a

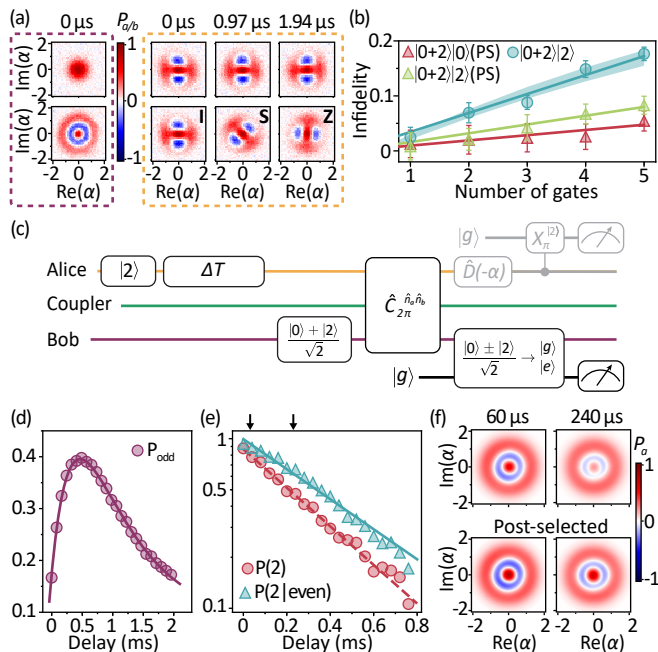


FIG. 4. **CPHASE on a biased-erasure code.** (a) Measured Wigner functions with Alice in $|0\rangle$ or $|2\rangle$, and Bob initialized in $\frac{|0\rangle+|2\rangle}{\sqrt{2}}$ for three different drive durations, corresponding to the controlled-I, S and Z gates. (b) Repeated application of C_π when the control is in $|0\rangle$ (red) or $|2\rangle$ (turquoise and green). Data are offset by the initial state preparation infidelity. Dots are raw experimental data, and triangles are data post-selected on the cavities being in even photon number after the protocol. When driving the gate, states acquire an infidelity of $3.9 \pm 0.5\%$ (turquoise), $1.2 \pm 0.5\%$ (green), and $0.6 \pm 0.2\%$ (red) per gate. Shaded region represents master equation simulations of dynamics given by Eq. 3. Spread corresponds to 10% variation of coherences. (c) Sequence to perform parity check via the engineered cross-Kerr. Alice, the storage mode, is initialized in $|2\rangle$, and allowed to decay for a variable duration up to 2 ms. Bob, the ancillary mode, is then prepared in $(|0\rangle + |2\rangle)/\sqrt{2}$, and a $C_{2\pi}$ gate is applied. The state of Bob is then mapped onto the ground/excited state of its auxiliary transmon with a SNAP pulse [39]. Finally, we perform full state tomography (gray) on Alice to verify the performance of the bosonic parity check. (d) Probability of measuring excited state of Bob’s auxiliary transmon. Open circles are the experimental data, with error bars smaller than the markers, and solid line the theoretical prediction calculated using the independently measured single-photon decay time of Alice, $T_1 = 800 \pm 10 \mu\text{s}$. (e) Population of Fock state $|2\rangle$ in Alice extracted from the reconstructed density matrix. A linear fit shows the decay constant with (red) and without (turquoise) post-selecting on the bosonic parity check result are $763 \pm 11 \mu\text{s}$ and $981 \pm 25 \mu\text{s}$, respectively. (f) Wigner plots of the reconstructed states in Alice at two different times marked, with (bottom) and without (top) post-selection based on the bosonic parity check via Bob.

memory state $|2\rangle$ in Alice and let it relax over a variable delay time, ΔT , between 0 and 2 ms before enacting a $C_{2\pi}$ gate between Alice and Bob, which is initialized in

$\frac{|0\rangle+|2\rangle}{\sqrt{2}}$. This operation maps the photon number parity information of Alice onto the phase of Bob, which is then probed by an auxiliary transmon via a selective number-dependent arbitrary phase (SNAP) [48] pulse that maps $\frac{|0\rangle+|2\rangle}{\sqrt{2}}$ ($\frac{|0\rangle-|2\rangle}{\sqrt{2}}$) to $|g\rangle$ ($|e\rangle$). The probability of Alice being in an odd parity state after a photon loss event, P_{odd} , which is equivalent to measuring Bob’s auxiliary transmon in $|e\rangle$, is shown in Fig. 4(d). As photon loss occurs, P_{odd} increases and peaks around ~ 0.5 ms. Beyond this duration, P_{odd} starts to decrease as Alice decays to $|0\rangle$ after experiencing two photon loss events, recovering an even parity state. This behavior is well predicted by the analytical model (purple line), where Alice has an intrinsic single-photon lifetime of $T_1 \approx 0.75 \pm 0.05$ ms. This is also consistent with our control experiment, where the decay rate of $|2\rangle$ is directly measured using Alice’s auxiliary transmon (red line in Fig. 4(e)). The effective T_1 of Alice increases to 0.98 ms when we perform the bosonic parity check and post-select on Bob’s auxiliary transmon in $|g\rangle$ (turquoise line in Fig. 4(d)). We qualitatively verify this enhancement by plotting the Wigner functions of the reconstructed density matrices of Alice at two different delay times, $60 \mu\text{s}$ and $240 \mu\text{s}$ in Fig. 4(f). They indicate that our bosonic parity check effectively preserves the Wigner negativity of $|2\rangle$, which is otherwise significantly eroded by photon loss. The capability of performing such a bosonic parity check, without exposing the oscillator to any interactions outside the code space, is a crucial ingredient for effective syndrome extraction in bosonic QEC and realization of fault-tolerant algorithms.

Our implementation presents a first step towards engineering direct nonlinear couplings between oscillators and harnessing them for fault-tolerant bosonic information processing. The results reported here can be significantly improved with existing techniques to make it a valuable multi-purpose tool in bosonic cQED. In its current form, the dispersive coupling between the coupler and the oscillators leads to small variations in the effective coupling strengths for different Fock states. This can be readily corrected via active cancellation techniques [49, 50], multi-tone drives as used in related implementations [28, 51], or by a judicious choice of operating point that minimizes the resulting inhomogeneity across Fock states [35]. In addition, a promising alternative is to replace the transmon coupler with one that does not impart any dispersive shifts, such as the Superconducting Nonlinear Asymmetric Inductive eLement (SNAIL) [39, 52]. The primary limitation of the current gate fidelity is the drive-induced photon loss of the oscillators and the dressed dephasing arising from the interplay between the enhanced photon loss and the engineered cross-Kerr [39]. This is a known challenge in four-wave mixing architectures operating under strong drives [31, 43], and several mitigation strategies are available. Using the SNAIL would reduce the four-wave-mixing terms and suppress the decoherence stemming from these spurious dynamics. Alternatively, fast-flux

schemes could be used to dynamically tune the coupler to the operating point where the Raman condition is satisfied, eliminating drive-induced decoherence entirely [53].

In conclusion, our work demonstrates a dynamically activated cross-Kerr interaction between two superconducting cavities two orders of magnitude stronger than the residual always-on interaction and without exciting the nonlinear coupler. We leverage this direct non-linear coupling between the oscillators to generate a continuous CPHASE gate in the 0/1 and 0/2 photon subspaces, with gate fidelities exceeding 95%. Furthermore, we leverage this engineered cross-Kerr dynamics gate to implement a direct bosonic parity check, where photon loss of a storage cavity is detected via another ancillary oscillator mode, without ever directly interacting with a nonlinear auxiliary qubit. This suppresses any ancilla-induced decoherence mechanisms and ensures that the storage oscillator remains entirely within the protected bosonic code space during the syndrome measurement. These results present the first direct cross-Kerr interaction between two harmonic oscillators realized without explicitly populating nonlinear coupling elements. This work aligns with the emerging paradigm where nonlinear elements act solely as ancillary couplers [37, 54–56], while quantum information is stored in long-lived harmonic modes. Importantly, the resulting CPHASE gate we demonstrated is natively compatible with the full family of rotationally-symmetric codes and provides a critical ingredient for fault-tolerant QEC protocols [40]. Thus, the use cases demonstrated here, together with clear paths to mitigate the main limiting factors, establish our technique as a new primitive for the general bosonic quantum computing toolbox both in cQED and beyond.

Acknowledgments We acknowledge the funding support from the Singapore Ministry of Education (MOE-T2EP50222-0017) and The University of Sydney - National University of Singapore 2026 Ignition Grants. A.C., A.K., S.Q., acknowledge the support of the Singapore National Quantum Scholarship Scheme (NQSS). We thank Mr. Nixon Yang, Mr. Juncheng Man, and Dr. Yao Lu for technical inputs during the project development.

Supplementary information: A direct controlled-phase gate between microwave photons

S1. EXPERIMENTAL DEVICE AND SYSTEM PARAMETERS

The experimental device used in this work consists of two oscillators in the form of the standard three-dimensional stub cavities, Alice and Bob, machined out of high-purity (4N6) aluminum. They are coaxial $\lambda/4$ -resonators with cut-off frequencies around $f_{\text{cut}} \sim 600$ MHz and stub lengths at ~ 16.5 mm and ~ 15.3 mm, which correspond to frequencies of 4.12 GHz and 4.41 GHz, respectively. The external surface layer (~ 0.15 mm) of the device has been chemically removed with aluminium etchant type A to reduce fabrication imperfections, achieving Q factors of $\sim 2 \cdot 10^7$ and $\sim 3 \cdot 10^7$, respectively. Each oscillator is capacitively coupled to a standard auxiliary transmon that is used for state preparation and readout. The electromagnetic field distributions were simulated using Ansys HFSS, and the Hamiltonian parameters were determined using the energy participation ratio (EPR) approach provided by the python package pyEPR [57]. The Hamiltonian of both cavities and their side chips has the form

$$\begin{aligned} H_i/\hbar = & \omega_i \hat{i}^\dagger \hat{i} + \omega_{q_i} \hat{q}_i^\dagger \hat{q}_i + \omega_{rr_i} \hat{r}_i^\dagger \hat{r}_i \\ & - \frac{\alpha_{q_i}}{2} \hat{q}_i^\dagger \hat{q}_i^\dagger \hat{q}_i \hat{q}_i - \frac{K_i}{2} \hat{i}^\dagger \hat{i}^\dagger \hat{i} \hat{i} \\ & - \chi_{i q_i} \hat{i}^\dagger \hat{i} \hat{q}_i^\dagger \hat{q}_i - \chi_{q_i rr_i} \hat{q}_i^\dagger \hat{q}_i \hat{r}_i^\dagger \hat{r}_i, \end{aligned} \quad (\text{S1})$$

where $\hat{i} = \hat{a}, \hat{b}$, for both oscillators. All the parameters of the Hamiltonian and their physical meaning are summarized in table S1.

To allow for fast initial state preparation and fast tomography, both oscillators couple to the respective auxiliary transmons in the strong dispersive coupling regime. The strength of this dispersive coupling is chosen such that the inherited self-Kerr non-linearity of the cavity modes, $K_{a/b}$, is in an acceptable range of 1-3 kHz. All the states used in the main text are prepared using numerically optimized Gradient Ascent Pulse Engineering (GRAPE) pulses [58] of $2 \mu\text{s}$ length. Tomography is performed either by sampling the Wigner function and measuring the parity of the cavity state at different points in phase space using a standard Ramsey technique, or by using the Optimized Reconstruction via excitation number sampling (ORENS) technique [59]. Further details are presented in Section S9 below.

A. Coupler frequency arrangement

Both oscillators are capacitively coupled to a flux-tunable asymmetric Superconducting Quantum Interfer-

Parameter	Description	Value
$\omega_a/2\pi$	Alice frequency	4.12 GHz
$\omega_{q_a}/2\pi$	Transmon A frequency	5.65 GHz
$\omega_{rr_a}/2\pi$	Resonator A frequency	7.20 GHz
$\alpha_{q_a}/2\pi$	Transmon A anharmonicity	118.3 MHz
$K_a/2\pi$	Alice self-Kerr	1.3 kHz
$\chi_{a q_a}/2\pi$	Transmon A - Alice disp. shift	0.77 MHz
$\chi_{q_a rr_a}/2\pi$	Transmon A - Resonator A disp. shift	0.6 MHz
$\omega_b/2\pi$	Bob frequency	4.41 GHz
$\omega_{q_b}/2\pi$	Transmon B frequency	5.18 GHz
$\omega_{rr_b}/2\pi$	Resonator B frequency	7.32 GHz
$\alpha_{q_b}/2\pi$	Transmon B anharmonicity	137.9 MHz
$K_b/2\pi$	Bob self-Kerr	2.4 kHz
$\chi_{b q_b}/2\pi$	Transmon B - Bob disp. shift	2.16 MHz
$\chi_{q_b rr_b}/2\pi$	Transmon B - Resonator B disp. shift	0.45 MHz
$\omega_c/2\pi$	Coupler frequency	5.22 GHz
$\alpha_c/2\pi$	Coupler anharmonicity	196 MHz
$\chi_a/2\pi$	Coupler - Alice disp. shift	0.8 MHz
$\chi_b/2\pi$	Coupler - Bob disp. shift	0.5 MHz
$\omega_{rr_c}/2\pi$	Coupler readout frequency	7.49 GHz
$\chi_{c rr_c}/2\pi$	Coupler - readout disp. shift	0.8 MHz

TABLE S1. **Hamiltonian parameters of the device.** The parameters of the coupler and its readout resonator correspond to the the operating flux-bias point used in Figures 3 and 4 of the main text.

ence Device (SQUID) [60] that acts as the coupler in these experiments. While flux-tunability is not strictly necessary for our protocol, it provides the flexibility to avoid frequency configurations with unexpected higher order transitions, as well as to explore different coupler frequencies within the same cooldown.

As the auxiliary transmons do not participate in the main dynamics of the engineered cross-Kerr coupling, we now focus only on the Hamiltonian of the coupler and both oscillators, given by:

$$\begin{aligned} H_c/\hbar = & \omega_a \hat{a}^\dagger \hat{a} - \frac{K_a}{2} \hat{a}^\dagger \hat{a}^\dagger \hat{a} \hat{a} \\ & + \omega_b \hat{b}^\dagger \hat{b} - \frac{K_b}{2} \hat{b}^\dagger \hat{b}^\dagger \hat{b} \hat{b} \\ & + \omega_c \hat{c}^\dagger \hat{c} - \frac{\alpha_c}{2} \hat{c}^\dagger \hat{c}^\dagger \hat{c} \hat{c} \\ & - \chi_a \hat{a}^\dagger \hat{a} \hat{c}^\dagger \hat{c} - \chi_b \hat{b}^\dagger \hat{b} \hat{c}^\dagger \hat{c} - \frac{K_{ab}}{2} \hat{a}^\dagger \hat{a} \hat{b}^\dagger \hat{b} \\ & + \omega_{rr_c} \hat{r}^\dagger \hat{r} - \chi_{c rr_c} \hat{c}^\dagger \hat{c} \hat{r}^\dagger \hat{r}, \end{aligned} \quad (\text{S2})$$

where the experimental parameters associated with each mode used in Figures 3 and 4 in the main text are summarized in table S1.

To engineer the Raman-assisted interaction described in the main text, we must parametrically drive the coupler at a frequency $\omega_d \approx \omega_c \pm |\omega_b - \omega_a|$. Drive frequencies

closer to the coupler generally relate to a stronger Stark Shift on the coupler mode, which indicates a higher effective drive strength ξ . Thus, we designed the oscillator frequencies ω_a and ω_b at close spectral proximity $\omega_b - \omega_a \approx 2\pi \cdot 284$ MHz. Since this detuning is comparable to the coupler anharmonicity, we chose to drive the $a^\dagger b|g\rangle\langle e| + h.c.$ rather than the $ab^\dagger|g\rangle\langle e| + h.c.$, in order to avoid driving the coupler in its straddling regime. Both processes would however, in principle, generate the desired cross-Kerr interaction.

Placing the coupler on top of the cavities allows us to tune the coupling regime of the system from essentially decoupled to almost resonant, as we increase the biasing flux. In general, frequencies close to the cavities proved to be inadequate as they resulted in an increase in the always-on native cross-Kerr, effectively decreasing the on/off ratio of the gate. Frequencies closer to the readout resonator yielded the worst dephasing times for the whole system, likely due to photon shot noise caused by residual populations in the coupler and readout mode. However, the strength of the coherent exchange interaction g_1 is directly proportional to the dispersive shift of both cavities, as described in the main text. Thus, we must consider the tradeoff between biasing the coupler to have a potentially fast gate and keeping the always-on cross-Kerr between the cavities K_{ab} below the kHz level to preserve the high on-off ratio of the gate. Balancing these considerations, we primarily explored the coupler frequency range of 5.1 ± 0.2 GHz.

B. Coupler flux delivery

Introducing magnetic flux while preserving the coherence of a superconducting cavity is highly non-trivial [61]. Here, we follow the approach in [37], where an on-chip superconducting pick-up loop [36] transfers flux from a nearby magnetic coil to the SQUID. The loop works as a transformer, where the magnetic flux originating from a small superconducting coil threads the pick-up loop, inducing a screening current which then biases the SQUID loop.

The magnetic coil generating the initial magnetic field consists of ~ 500 turns of NbTi superconducting wire (SC-54S43-0.178 mm wire from Supercon) coiled around an OFHC copper spool of 1 cm length and 4.5 mm diameter. The terminals of the coil are soldered to the DC lines at the mixing chamber (MXC) stage of the dilution refrigerator. The spool is thermally anchored to the lid of the cavities, which is also made of OFHC copper, and is thermally anchored directly to the MXC stage using a copper braid. We observed a maximum MXC stage temperature of 26 mK when passing a current of 60 mA.

The design of the SQUID chip is shown in Fig. S1(a). The geometry of the pick-up loop was optimized using Ansys Maxwell to maximize the flux delivered to the device while minimizing the current required in the coil. Further, we also verified in simulation that the design

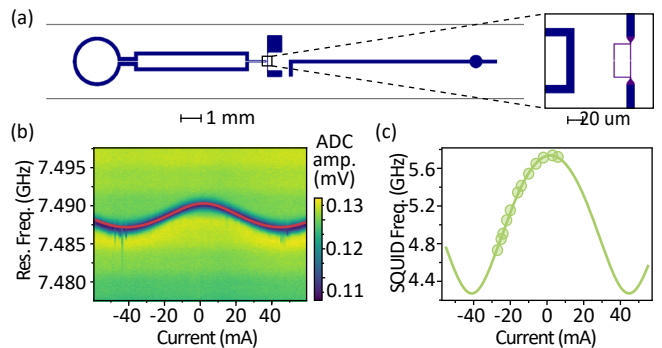


FIG. S1. **Tunable SQUID coupler.** (a) Layout of the SQUID coupler chip, with the pick-up loop transformer (left), the SQUID (middle), and its readout resonator (right). (b) Readout frequency as a function of the current applied to bias the SQUID. Solid line shows the fit used to extract the current-flux relation. (c) SQUID frequency as a function of current. Solid line shows the fitted frequency.

protects the Q factors of both cavities and does not introduce undesired modes in the system. The final configuration consists of 4 distinct sections: (i) a circular region optimized to only collect the magnetic flux piercing the chip; (ii) a constriction to avoid collecting the returning field; (iii) two separated loop arms that reduce the loop self-inductance; and (iv) a narrowed section near the SQUID loop that avoids interference with the junction fabrication during lithography. The length of the pick-up loop was chosen to balance two effects. First, it needs to be long enough such that the copper coil and spool are spatially separated from the cavities. This geometric constraint prevents the electric field of the cavity TEM modes from leaking out through the aperture of the coil and preserves the cavity lifetimes. Secondly, this loop design introduces parasitic resonant modes, currently at 6.2 GHz and 8.1 GHz, which decrease in frequency as the transformer length increases, potentially interfering with the other modes of the system. Finally, our SQUID loop spreads over an area of $800 \mu\text{m}^2$, and is placed at a distance of $\sim 50 \mu\text{m}$ from the flux transformer, see inset in Fig. S1(a). The transformer has a width of $10 \mu\text{m}$ at its narrowest point, ensuring that it remains superconducting even at large induced currents.

Given the large loop area, we anticipated that the coherence of the SQUID coupler would likely be limited by flux noise. To mitigate this, we used an asymmetric SQUID, which generally exhibits less sensitivity to dephasing. Given the junction Josephson energies E_{J_1} and E_{J_2} , the effective Josephson energy of the SQUID is

$$E_J(\Phi_{\text{ext}}) = E_{J,\Sigma} \cos\left(\pi \frac{\Phi_{\text{ext}}}{\Phi_0}\right) \sqrt{1 + \frac{E_{J,\Delta}}{E_{J,\Sigma}} \tan^2\left(\pi \frac{\Phi_{\text{ext}}}{\Phi_0}\right)} \quad (\text{S3})$$

where $E_{J,\Sigma} = E_{J_1} + E_{J_2}$ and $E_{J,\Delta} = E_{J_1} - E_{J_2}$.

The measured frequency of the asymmetric SQUID as a function of the applied current on the coil can be seen

in Fig.S1(c). Due to the increased attenuation of the drive line at lower frequencies and the reduced coupling to its readout resonator, we could not measure the coupler frequency for values below 4.7 GHz. By fitting the SQUID readout resonator frequency as a function of the applied current through the coil, we can extract the relation between the current and the flux in the SQUID loop, with 42.89 mA corresponding to half a flux quantum, see Fig. S1(b). Finally, to extract the whole tunability range and the individual Josephson energies, E_J , of both junctions, we consider the coupler-resonator Hamiltonian,

$$\hat{H}_c/\hbar = 4E_C\hat{n}^2 - E_J(\Phi_{\text{ext}}) \cos \hat{\phi} + \omega_{rr_c} \hat{r}^\dagger \hat{r} + g(\hat{c} - \hat{c}^\dagger)(\hat{r} - \hat{r}^\dagger), \quad (\text{S4})$$

where E_C is the charging energy of the SQUID, \hat{n} its the charge operator, $\hat{\phi}$ its phase operator, ω_{rr_c} the readout resonator frequency and g the SQUID-resonator coupling strength. Fitting the frequencies of these two modes, constrained with the measured anharmonicity and the current-flux relation, we obtain the parameters shown in Table S2. This allows us to determine the full SQUID tunability, spanning 4.3 GHz to 5.7 GHz (solid line in Fig.S1(c)), as well as the SQUID asymmetry, $E_{J_1}/E_{J_2} \approx 3.7$, which closely matches the designed asymmetry during fabrication. These are the parameters used in the Floquet simulations discussion in Section S5.

Parameter	Value	Description
E_{J_1}	19.0 ± 0.1 GHz	Josephson energy
E_{J_2}	5.2 ± 0.1 GHz	Josephson energy
E_C	181.4 ± 0.1 MHz	Charging energy
c	0.0112 ± 0.0002 mA ⁻¹	Flux-current relation
Φ_{ext}	-0.068 ± 0.006	External flux
g	0.10 ± 0.02 GHz	Coupling constant
ω_{r_0}	7.484 ± 0.002 GHz	Resonator frequency

TABLE S2. **Hamiltonian parameters of the SQUID coupler.** Parameters were fitted to reproduce the resonator and coupler flux tunability as a function of the applied current, with the additional constrain of reproducing the experimental anharmonicity of the coupler.

C. System coherences

Each transmon and their readout resonator are addressed through the same coupling port, whose location has been optimized in Ansys HFSS to suppress the radiative decay of the transmons into the measurement lines, achieving an intrinsic Purcell filter [62] that preserves their coherences. Avoiding on-chip Purcell filters helps in decreasing the length of the chips, making them less susceptible to vibrations and allowing a more compact device. Their coherence times are shown in Table S3. The coupler coherence times depend strongly on the applied flux bias, with T1 times ranging from 50 μ s at the lowest-measured frequencies to 10 μ s at its sweet spot, where the coupler hybridizes more strongly with its readout resonator. On the other hand, the dephasing times

range from up to 20 μ s at the flux sweet spot to 1 μ s at the most sensitive spot. The coupler coherence times in the configuration used to obtain the final data for Figures 3 and 4 in the main text are shown in Table S3. Although the coupler is operated near its most flux-sensitive point during the protocol, its intrinsic decoherence does not play a significant role, as the Raman-assisted interaction is mediated through virtual processes that avoid population of its excited states.

Param.	Value (μ s)	Param.	Value (μ s)	Param.	Value (μ s)
T_{1q_a}	25	T_{1q_b}	50-60	T_{1c}	50
$T_{2q_a}^*$	18	$T_{2q_b}^*$	40-50	T_{2c}^*	2.5
$T_{2q_a}^E$	22	$T_{2q_b}^E$	50	T_{2c}^E	10
T_{1a}	700-900	T_{1b}	800-1000		
T_{2a}	500-600	T_{2b}	700-900		

TABLE S3. **Coherence times of the device.** Coherence times for the coupler are quoted at the flux point used in the main text. Transmon T_2^* were measured with a standard Ramsey technique and T_2^E with a Hahn-echo experiment. Oscillator T_1 times were measured by fitting the decay of both coherent states and single photons. Oscillator T_2 times were measured through a Ramsey experiment using SNAP pulses.

In contrast, cavity decoherence is the direct limiting factor to the quality of our engineered cross-Kerr. The coupling ports of the cavities are designed to have quality factors $\sim 10^9$ to suppress decay through them. Good care was also taken to minimize the cavity photon field from leaking into the coil used to bias the SQUID. We measured cavity T_1 times both by initializing a coherent state and measuring its characteristic decay, and by loading a photon in the cavity using SNAP pulses and fitting an exponential decay. Both methods give consistent results with single-photon lifetimes of 700 μ s and 900 μ s for Alice and Bob, respectively. The cavity T_2 times were measured using a standard Ramsey technique. The cavity is initialized in the state $\frac{1}{\sqrt{2}}(|0\rangle + |1\rangle)$ using SNAP pulses, followed by a variable wait time. The state is then displaced by $D(\alpha = -0.8e^{i\omega t})$, which maximizes overlap with the vacuum state for $|0\rangle + |1\rangle$ and minimizes it for $|0\rangle - |1\rangle$. We also include a fixed virtual detuning and we extract the T_2 dephasing time by fitting the data to an exponentially decaying sinusoid

D. Auxiliary transmon readout

Both the auxiliary transmons and the SQUID coupler are measured using Cavity Level Excitation and Reset (CLEAR) readout pulses [63] applied to their respective readout resonators. In contrast to a conventional constant-amplitude readout pulse, the CLEAR protocol employs a sequence of five piecewise-constant segments: two ring-up segments, one steady-state segment, and two ring-down segments. This pulse shaping offers high-fidelity state discrimination while significantly reducing residual photon population after measurement.

Compared to standard square pulses, CLEAR pulses achieve faster resonator reset and therefore support reduced measurement-induced backaction and shorter experimental cycle times. The amplitudes and duration of the individual CLEAR drive segments are optimized running an algorithm that minimizes the population of the resonator after the CLEAR pulse given the decay time of the resonator $1/\kappa$ and the dispersive shift to the qubit χ .

In addition to CLEAR pulse shaping, our readout is typically optimized to differentiate between $|g\rangle$ and $|f\rangle$, which improves the separation of the histogram counts for the same integration time compared to discriminating between $|g\rangle$ and $|e\rangle$, as $\chi_{gf} \approx 2\chi_{ge}$. After each experimental sequence we map the $|e\rangle$ population to the $|f\rangle$ state using a gaussian pulse of $\sigma = 24$ ns. The resulting confusion matrices for both auxiliary transmons used in the tomography and state preparation steps are:

$$M_{\text{RO},A} = \begin{pmatrix} P(g|g) = 97.5\% & P(e|g) = 2.5\% \\ P(g|e) = 2.8\% & P(e|e) = 97.2\% \end{pmatrix}$$

$$M_{\text{RO},B} = \begin{pmatrix} P(g|g) = 95.9\% & P(e|g) = 4.1\% \\ P(g|e) = 6.4\% & P(e|e) = 93.6\% \end{pmatrix}$$

E. Chip fabrication

The ancillary transmon chips and the SQUID coupler chip are fabricated in aluminum on a sapphire substrate. A HEMEX sapphire wafer is cleaned in a 2:1 piranha solution for 20 minutes and rinsed in de-ionized (DI) water for 20 minutes, then quickly rinsed in methanol and blown-dry with nitrogen. The wafer is coated with 700 nm of MMA and 200 nm of PMMA resist by spinning it for 100 seconds at 2000 rpm and baking it for 5 minutes at 200°C.

A ~ 10 -nm discharge gold layer is sputtered in a Cressington sputterer at 30 mA for 30 seconds. The design is patterned using a Raith electron-beam lithography machine. The gold layer is removed in a KI solution and rinsed in DI water, prior to developing the resist in a 3:1 mixture of DI water and isopropanol. The wafer is then loaded into an Angstrom Engineering double-angle evaporator and pumped to 10^{-8} mbar, after which the resist is ion milled in a mixture of 85% O₂ and 15% Argon, at 400 V for 15 s at -20° and 15 s at 20° to clean any resist residues. We deposit two aluminum layers of 20 nm and 30 nm thickness at -20° and $+20^\circ$, respectively, separated by an oxidation step with a mixture of 85% O₂ and 15% Argon at 20 mbar for 20 minutes, and a final capping layer with the same oxidation conditions. The remaining resist is lifted off in NMP at 90°C for 3 hours, then rinsed in acetone and methanol. Finally, a protective layer of AZ1512 photoresist is spun at 2000 rpm and baked at 80°C for 1 minute, and the individual chips are diced on an Accretech machine with a resin blade

at 15000 rpm. The chips are finally cleaned in NMP, acetone and methanol, blown-dry and inserted into the waveguides using an aluminum clamp with indium wire to improve thermalization.

S2. SNAP PULSES

We use Selective Number-dependent Arbitrary Phase (SNAP) gates [48] to prepare the oscillators in Fock state $|1\rangle$ and the superposition state $|0+1\rangle$, respectively to measure the single-photon decay rate and dephasing rate of the oscillators. The SNAP pulses consist of an initial displacement of the oscillators by α_1 , a θ_n phase imparted on the transmon state conditioned on the oscillator having n photons, and a final displacement of the oscillators by α_2 . All parameters used can be found in Table S4. Oscillator displacements were performed using 100 ns constant pulses with 32 ns cosine ramps at the resonant frequency of the oscillators. The conditional phases $\theta_n = \pi$ were realized by driving the transmons through a full 2π Bloch sphere rotation using gaussian pulses of $\sigma_a = 960$ ns and $\sigma_b = 400$ ns, applied at the resonance frequency of each transmon conditioned on the oscillator containing n photons.

Transition	α_1	θ_0	θ_1	α_2
$ 0\rangle \rightarrow 1\rangle$	1.14	π	0	-0.58
$ 0\rangle \rightarrow \frac{ 0\rangle+ 1\rangle}{\sqrt{2}}$	0.56	π	0	-0.24
$\frac{ 0\rangle- 2\rangle}{\sqrt{2}} \rightarrow 0\rangle$	-0.35	π	π	1.04

TABLE S4. **Different SNAP parameters used in the main text.** First row corresponds to the creation of a single photon in the oscillators, used to measure their decay time. Second row corresponds to the creation of a superposition state in the oscillators, used to measure their dephasing time in a Ramsey experiment. Last row corresponds to the pulse used in the direct cavity-cavity parity mapping, shown in Fig. 4(c) in the main text.

For the cavity-cavity parity mapping described in Fig. 4(c) in the main text, we use a SNAP pulse that maps the relevant states of Bob as

$$\begin{aligned} \frac{|0\rangle - |2\rangle}{\sqrt{2}} &\rightarrow |0\rangle \\ \frac{|0\rangle + |2\rangle}{\sqrt{2}} &\rightarrow 0.9|1\rangle + 0.4|2\rangle + \dots \end{aligned}$$

Hence, a selective π -pulse to Bob's auxiliary transmon conditioned on Bob being in vacuum, maps $\frac{|0\rangle-|2\rangle}{\sqrt{2}}$ ($\frac{|0\rangle+|2\rangle}{\sqrt{2}}$) to $|e\rangle$ ($|g\rangle$). The numerical displacements to implement this transformation were found by a Nelder-Mead optimization that maximizes the probability of the final states ending either in vacuum or not in vacuum. The parameters of this SNAP sequence are specified in the last row of Table S4.

S3. WIRING DIAGRAM

The microwave signals to drive the oscillators, auxiliary transmons, coupler, and readout resonators of our device are directly generated from digital waveforms via Direct-Digital-Synthesis (DDS) by a Digital-to-Analog Converter (DAC) of a Quantum Machines OPX1000 Field-Programmable Gate Array (FPGA). We also place band-pass filters at the output line of the OPX1000, which increased the transmon coherence times significantly. Additionally, a RF switch (HMC-C058) placed on the coupler line provides an additional layer of noise protection. Importantly, most of the coupler drive line attenuation at the MXC stage is replaced by a Mini-circuits 5500+ low-pass filter and Mini-circuits 5500+ high-pass filter, which provide -30 dB attenuation at 5.0 GHz but only -10 dB at 5.5 GHz to be able to drive the coupler strongly, while still providing at least 60 dB attenuation at the oscillator frequencies and 35 dB at the resonator frequency.

Readout is performed using the standard reflection technique. The reflected signal, amplified by a High-Electron mobility transistor (HEMT - LNF-LNC48C) as well as a ZVA-183-S+ room temperature amplifier, is directly sampled by a high-speed Analog-to-Digital Converter (ADC) of the OPX1000 FPGA. The digital signal is then downconverted and separated into I and Q components. The DC current sent to the coil is generated in a YOKOGAWA GS200 DC voltage/current source. To shield our device from external electromagnetic noise it is placed in a standard Cryoperm shield and anchored directly at the MXC plate. The schematic of the wiring can be seen below in Fig. S2

S4. ANALYTICAL DERIVATION OF THE ENGINEERED DYNAMICS

The Hamiltonian of the two oscillators and the SQUID coupler is (setting $\hbar = 1$):

$$H(t)/\hbar = \tilde{\omega}_a \hat{a}^\dagger \hat{a} + \tilde{\omega}_b \hat{b}^\dagger \hat{b} + \tilde{\omega}_c \hat{c}^\dagger \hat{c} - E_J(\Phi_{\text{ext}}) \left(\cos \hat{\Phi} + \frac{1}{2!} \hat{\Phi}^2 \right) + \epsilon(t)(\hat{c} + \hat{c}^\dagger), \quad (\text{S5})$$

where $\tilde{\omega}_a$ and $\tilde{\omega}_b$ are the bare (uncoupled) oscillator frequencies, $\tilde{\omega}_c = \sqrt{8E_J(\Phi_{\text{ext}})E_C}$ is the Josephson plasma frequency of the coupler, $\epsilon(t)$ is the time-dependent drive on the coupler and

$$\hat{\Phi} = \phi_c (\hat{c} + \hat{c}^\dagger) + \phi_a (\hat{a} + \hat{a}^\dagger) + \phi_b (\hat{b} + \hat{b}^\dagger)$$

is the quantized phase of the coupler, that considers the participation of both oscillator fields in the junction.

The zero-point fluctuation of the coupler in the junction is defined as $\phi_c = \left(\frac{2E_C}{E_J(\Phi_{\text{ext}})} \right)^{1/4}$, and the zero-point

fluctuations of the oscillators in the junction are given by $\phi_a \approx \frac{g_a}{\Delta_a} \phi_c$ and $\phi_b \approx \frac{g_b}{\Delta_b} \phi_c$. Considering a drive $\epsilon(t) = 2 \epsilon \cos(\omega_d t + \phi_d)$, we can go to the displaced frame $q \rightarrow q + \xi e^{-i\omega_d t}$ with $\xi = \frac{\epsilon}{\omega_d - \tilde{\omega}_c}$, where the drive term is absorbed into the phase variable through

$$\hat{\Phi} = \phi_c (\hat{c} + \hat{c}^\dagger + \xi e^{-i\omega_d t} + \xi^* e^{i\omega_d t}) + \phi_a (\hat{a} + \hat{a}^\dagger) + \phi_b (\hat{b} + \hat{b}^\dagger).$$

By expanding the cosine in Eq.S5 up to fourth order in $\hat{\Phi}$, and keeping all the terms that are naturally on-resonance, we obtain the full Hamiltonian of the system

$$\begin{aligned} \hat{H}_0 = & \omega_a \hat{a}^\dagger \hat{a} - \frac{K_a}{2} \hat{a}^\dagger \hat{a}^\dagger \hat{a} \hat{a} \\ & + \omega_b \hat{b}^\dagger \hat{b} - \frac{K_b}{2} \hat{b}^\dagger \hat{b}^\dagger \hat{b} \hat{b} \\ & + \omega_c \hat{c}^\dagger \hat{c} - \frac{\alpha}{2} \hat{c}^\dagger \hat{c}^\dagger \hat{c} \hat{c} \\ & - \chi_a \hat{a}^\dagger \hat{a} \hat{c}^\dagger \hat{c} - \chi_b \hat{b}^\dagger \hat{b} \hat{c}^\dagger \hat{c} - K_{ab} \hat{a}^\dagger \hat{a} \hat{b}^\dagger \hat{b}, \end{aligned} \quad (\text{S6})$$

where K_a and K_b are the cavity self-Kerrs inherited from the coupler non-linearity, α is the coupler non-linearity (anharmonicity), χ_a and χ_b are the coupler-cavity cross-Kerrs (dispersive shifts), and K_{ab} is the residual always-on cavity-cavity cross-Kerr. All these terms produce Lamb and Stark shifts on the bare mode frequencies, which get renormalized as

$$\begin{aligned} \omega_a = & \tilde{\omega}_a - \frac{\chi_a}{2} - K_a - \frac{K_{ab}}{2} - \chi_a |\xi|^2 \\ \omega_b = & \tilde{\omega}_b - \frac{\chi_b}{2} - K_b - \frac{K_{ab}}{2} - \chi_b |\xi|^2 \\ \omega_c = & \tilde{\omega}_c - \alpha - \frac{\chi_a}{2} - \frac{\chi_b}{2} - 2\alpha |\xi|^2, \end{aligned}$$

where the last term of each equation corresponds to the drive-induced AC Stark shifts.

By moving to a frame rotating at $\omega_a \hat{a}^\dagger \hat{a} + \omega_b \hat{b}^\dagger \hat{b} + \omega_c \hat{c}^\dagger \hat{c}$ and restricting the qubit basis to the first two energy levels $\{|g\rangle, |e\rangle\}$, we find that a drive frequency at

$$\omega_d = \omega_c + \omega_b - \chi_b - \omega_a + \Delta, \quad (\text{S7})$$

where Δ is the detuning to the resonance condition, successfully activates the dynamics given by

$$H_d(t) = g_1 e^{it\Delta} \hat{a}^\dagger \hat{b} |g\rangle \langle e| + g_1^* e^{-it\Delta} \hat{a} \hat{b}^\dagger |e\rangle \langle g|, \quad (\text{S8})$$

which corresponds to Eq.2 in the main text. The strength of this interaction is given by

$$g_1 = E_J \phi_c^2 \phi_a \phi_b \xi^* \approx \sqrt{\chi_a \chi_b} \xi^*. \quad (\text{S9})$$

We measured the coherent exchange rate, g_1 , for different effective drive strengths $|\xi|$ obtained from the coupler AC Stark shift, as shown in Fig. S3(a). The slope of the interaction rate is in very good agreement with the prediction of Eq.S9 using the experimentally measured dispersive shifts (solid line).

To find an analytical equation for the engineered cross-Kerr, we diagonalize the interaction term of Eq. S8, by

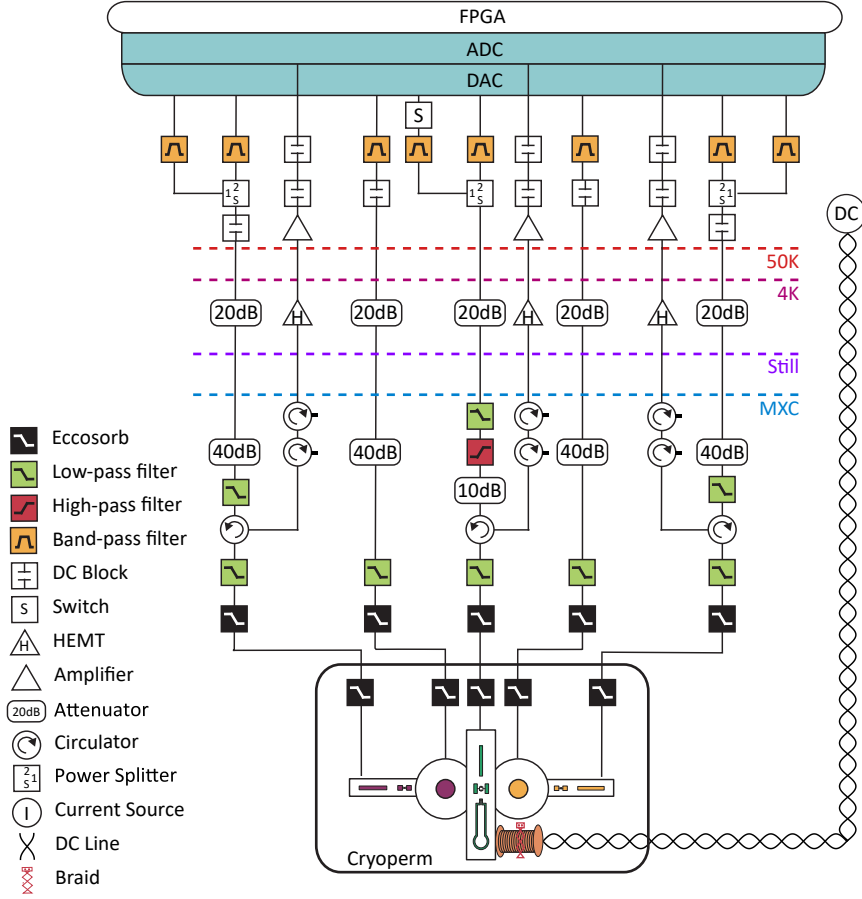


FIG. S2. **Experimental wiring setup.** Schematic of the RF components and connections at room temperature and inside the Bluefors dilution refrigerator. Most of the attenuation for the coupler drive line is replaced by a low-pass filter in series with a high-pass filter that act as at 5-7 GHz band-pass filter.

applying a time-independent Schrieffer-Wolff transformation (SWT) [38, 64] in the rotating frame of the drive. Note that this is equivalent to applying a time-dependent SWT in the rotating frame of the coupler, which is also equivalent to performing a second-order RWA [65].

In the rotating frame of the drive, the diagonal part of the Hamiltonian reads

$$\begin{aligned}
 \hat{H}'_0/\hbar = & \omega_a \hat{a}^\dagger \hat{a} - \frac{K_a}{2} \hat{a}^\dagger \hat{a}^\dagger \hat{a} \hat{a} \\
 & + \omega_b \hat{b}^\dagger \hat{b} - \frac{K_b}{2} \hat{b}^\dagger \hat{b}^\dagger \hat{b} \hat{b} \\
 & + (\omega_c - \omega_d) \hat{c}^\dagger \hat{c} - \frac{\alpha}{2} \hat{c}^\dagger \hat{c}^\dagger \hat{c} \hat{c} \\
 & - \chi_a \hat{a}^\dagger \hat{a} \hat{c}^\dagger \hat{c} - \chi_b \hat{b}^\dagger \hat{b} \hat{c}^\dagger \hat{c} - K_{ab} \hat{a}^\dagger \hat{a} \hat{b}^\dagger \hat{b},
 \end{aligned} \tag{S10}$$

and the perturbation is

$$\hat{V}/\hbar = g_1 \hat{a}^\dagger \hat{b} |g\rangle \langle e| + g_1^* \hat{a} \hat{b}^\dagger |e\rangle \langle g|. \tag{S11}$$

The SWT consists of finding an anti-Hermitian generator $\hat{S} = -\hat{S}^\dagger$ that satisfies

$$\hat{V} = [\hat{H}'_0, \hat{S}], \tag{S12}$$

which transforms the Hamiltonian to

$$\begin{aligned}
 \hat{H}' &= e^{\hat{S}} (\hat{H}'_0 + \hat{V}) e^{-\hat{S}} \\
 &= \hat{H}'_0 + \hat{V} + [\hat{S}, \hat{H}'_0] + [\hat{S}, \hat{V}] + \frac{1}{2!} [\hat{S}, [\hat{S}, \hat{H}'_0]] + \dots \\
 &\approx \hat{H}'_0 + \frac{1}{2} [\hat{S}, \hat{V}].
 \end{aligned} \tag{S13}$$

By choosing a generator of the form

$$\hat{S} = \beta (\hat{a}^\dagger \hat{b} |g\rangle \langle e| - \hat{a} \hat{b}^\dagger |e\rangle \langle g|), \tag{S14}$$

we can solve Eq. S12 to find the expression for β , which depends on the number of photons on both cavities, as given by

$$\left[\hat{H}'_0, \hat{a}^\dagger \hat{b} |g\rangle \langle e| \right] = (\omega_d - \omega_c + \omega_a - \omega_b - K_a(\hat{n}_a - 1) + K_b \hat{n}_b + \chi_a(\hat{n}_a - 1) + \chi_b(\hat{n}_b + 1) - K_{ab}(\hat{n}_b - \hat{n}_a + 1)) \hat{a}^\dagger \hat{b} |g\rangle \langle e|.$$

Therefore, the transformation generator is given by

$$\hat{S} = \sum_{n_a, n_b} \beta_{n_a n_b} (|n_a, n_b, g\rangle \langle n_a - 1, n_b + 1, e| - |n_a - 1, n_b + 1, e\rangle \langle n_a, n_b, g|), \quad (\text{S15})$$

with

$$\beta_{n_a n_b} = \frac{\sqrt{n_a(n_b + 1)} g_1}{\omega_d - \omega_c + \omega_a - \omega_b - K_a(n_a - 1) + K_b n_b + \chi_a(n_a - 1) + \chi_b(n_b + 1) - K_{ab}(n_b - n_a + 1)}. \quad (\text{S16})$$

Finally, solving Eq. S13 leads to

$$\hat{H}' = \hat{H}'_0 + \sum_{n_a, n_b} \beta_{n_a n_b} \sqrt{n_a(n_b + 1)} g_1 (|n_a, n_b, g\rangle \langle n_a, n_b, g| - |n_a - 1, n_b + 1, e\rangle \langle n_a - 1, n_b + 1, e|). \quad (\text{S17})$$

With these analytical results, we can see that when we parametrically drive this dynamics, the energies of the states $|1\rangle|0\rangle|g\rangle$ and $|1\rangle|1\rangle|g\rangle$ are shifted by

$$\Delta E_{10} = \frac{g_1^2}{\Delta}, \quad (\text{S18})$$

$$\Delta E_{11} = \frac{2g_1^2}{\Delta + \chi_b + K_b - K_{ab}} \approx \frac{2g_1^2}{\Delta + \chi_b}. \quad (\text{S19})$$

Eq. S18 shows that in presence of the parametric drive, despite Bob being in vacuum, the state $|+\rangle|0\rangle|g\rangle$ will acquire a phase at a rate ΔE_{10} . Hence, it is important to track the frame of the oscillators (on software) for any subsequent operation. For instance, this unconditional detuning is included in the displacement pulses used for Wigner tomography via a virtual detuning. The phase acquired by the state $|+\rangle|0\rangle|g\rangle$ was also experimentally measured as a function of the detuning Δ , see green markers in Fig. S3(b), which agrees with the prediction of Eq. S18 (solid line).

Finally, the total cross-Kerr induced in the 0/1 photon subspace is thus

$$\begin{aligned} g_{ab} &= E_{11} - E_{10} - E_{01} + E_{00} \\ &= -K_{ab} + \Delta E_{11} - \Delta E_{10} \\ &= -K_{ab} + \frac{g_1^2 \Delta - (\chi_b + K_b - K_{ab})}{\Delta \Delta + (\chi_b + K_b - K_{ab})}, \end{aligned} \quad (\text{S20})$$

where E_{ij} refers to the energy of the state $|ijg\rangle$ and K_{ab} is the always-on residual cross-Kerr. We measured the cross-Kerr g_{ab} by tracking the oscillations of $|+\rangle|1\rangle|g\rangle$ in the frame where $|+\rangle|0\rangle|g\rangle$ does not oscillate, at different drive powers for a fixed detuning of $\Delta = -5$ MHz, see blue markers in Fig. S3(c). Notice that at different drive powers, the AC Stark shifted frequency of the coupler is different, which subsequently modifies the coherent exchange frequency ω_e . The solid blue line corresponds to the analytical behavior of Eq. S20, which underpredicts

the measured interaction strength. We believe this discrepancy arises because the analytical modes does not account for the enhanced hybridization between the modes under the strong drive, which renormalizes the dispersive shifts and the detunings. A full Floquet simulation, as described in the next section, is then necessary to fully reproduce the experimental observation. We discuss this in detail in the following section.

Nevertheless, the analytical model qualitatively captures the asymmetric behavior of the engineered cross-Kerr between positive and negative detunings, see purple markers in Fig. S3(d). The green (yellow) dotted line corresponds to $-\Delta E_{10}$ ($+\Delta E_{11}$), which diverges at $\Delta = 0$ ($\Delta \approx -\chi_b$). The solid purple line is the sum of both, which qualitatively reproduces the main features observed in the experimental data. For a quantitative agreement, it is hence desirable to model the system with Floquet theory, as shown in Fig. 2(b) in the main text.

S5. FLOQUET SIMULATIONS

In the presence of strong parametric drives, the system is governed by a time-periodic Hamiltonian in which the drive-induced shifts of the energy level give rise to unintended multi-photon transitions between the oscillators and higher levels of the coupler, beyond the coherent exchange interaction considered analytically. This scenario is appropriately addressed within the Floquet formalism [55, 66, 67]. We perform Floquet simulations using a QuTiP python package [68] to analyze the effects of the parametric drive on the subsystem composed of the SQUID coupled to both cavities, ignoring the side auxiliary transmons. The Hilbert spaces were truncated to dimension $D = 12$ for the SQUID and $D = 4$ for the cavities. The full Hamiltonian considered in the the

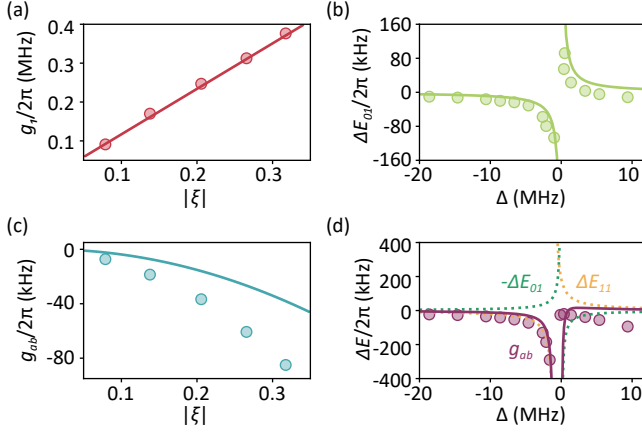


FIG. S3. **Analytical predictions based on the SWT.** (a) Coherent exchange rate, g_1 , as a function of the effective drive strength, $|\xi|$ (markers). The analytical prediction of Eq. S9 is in close agreement (solid line). (b) Phase rate acquired by the state $|+\rangle|0\rangle|g\rangle$ as a function of the detuning Δ to the coherent exchange condition. (c) Cross-Kerr strength (markers) measured at a fixed $\Delta = -5$ MHz, as a function of the drive powers. Analytical prediction (solid line) based on Eq. S20 underpredicts the strength by a factor of 2. (d) Cross-Kerr strength (markers) as a function of the detuning $\Delta = -5$ MHz. The purple line corresponds to the sum of the yellow and green lines, which exhibit discontinuities at $\Delta = 0$ and $\Delta \approx -\chi_b$, respectively.

simulation is

$$\begin{aligned}
 H/\hbar = & 4E_C \hat{n}^2 - E_J (\Phi_{\text{ext}}) \cos \hat{\phi} \\
 & + \omega_a \hat{a}^\dagger \hat{a} + \omega_b \hat{b}^\dagger \hat{b} \\
 & - g_{ac} (\hat{a}^\dagger - \hat{a})(\hat{c}^\dagger - \hat{c}) \\
 & - g_{bc} (\hat{b}^\dagger - \hat{b})(\hat{c}^\dagger - \hat{c}) \\
 & + \epsilon \cos(\omega_d t) (\hat{c}^\dagger + \hat{c}),
 \end{aligned} \tag{S21}$$

where the capacitive coupling strength between the oscillators and the SQUID were taken as $g_a/2\pi = 43.07$ MHz and $g_b/2\pi = 22.56$ MHz, to reproduce the experimentally measured dispersive shifts. Meanwhile the drive strength ϵ is calibrated to reproduce the coupler AC Stark shift. The rest of the parameters used in the simulation correspond to those in Table S2.

The resulting cross-Kerr strength as a function of drive detuning obtained from the Floquet simulation is consistent with our experimental observations as shown in Fig. 2 of the main text.

S6. CALIBRATION OF COHERENT EXCHANGE RATE

To confirm the location of the coherent exchange interaction, ω_e , and calibrate the exchange strength, g_1 , we measure the population of Alice, Bob, and the coupler, as a function of the drive duration and frequency (ω_d),

as shown in Fig. S4.

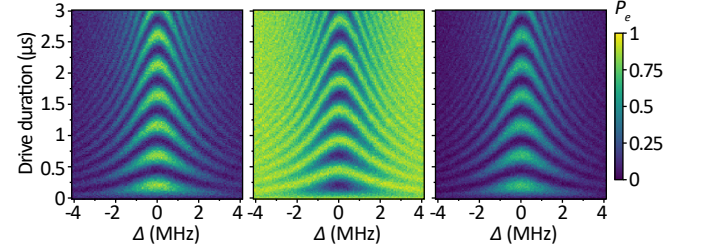


FIG. S4. **Coherent exchange of excitations between the coupler and the oscillators.** Left: probability of finding Alice in vacuum. Middle: probability of finding Bob in vacuum. Right: probability of the coupler being excited. System was initialized in $|1\rangle|0\rangle|g\rangle$. $\Delta = 0$ corresponds to $\omega_d = \omega_e$, where exchange occurs in ~ 200 ns. The coupler configuration corresponds to Fig. 2(a) in the main text.

The experiment starts by preparing the state $|1\rangle|0\rangle|g\rangle$ through a numerical GRAPE pulse on side qubit q_A and cavity A. A microwave drive is applied to the coupler with variable duration t and frequency ω_d . After the drive pulse, the system populations are measured. The coupler population is obtained via direct dispersive readout of its readout resonator, while the cavity populations are measured using cavity-selective π -pulses on the respective side qubits conditioned on the cavity being in the vacuum state. Therefore, the measured cavity signal corresponds to the cavity vacuum population and thus appears 'flipped' with respect to its actual population. The cavity data is normalized by the selective π -pulse contrast, while the coupler population is normalized by the readout contrast.

The data exhibits the characteristic chevron pattern expected for a coherent exchange between $|1\rangle|0\rangle|g\rangle$ and $|0\rangle|1\rangle|e\rangle$. At zero detuning, the populations oscillate sinusoidally in time with frequency $2g_1$ while detuning from the exchange condition leads to faster oscillations with reduced contrast. A line cut yields the oscillations shown in Fig. 2(a) of the main text, from which we can extract $g_1/(2\pi) = 1.024 \pm 0.004$ MHz.

S7. EXTENSION TO MULTI-PHOTON CODES

Due to the bosonic enhancement factor in the coupling strength, we can increase the gate speed by populating higher Fock states in the control cavity. We demonstrate this by measuring the phase acquired by the $|+\rangle$ state during gate operation when the control cavity is in $|2\rangle$ and comparing it to the equivalent case when the control is in $|1\rangle$. The phases acquired as a function of time for both cases are shown in Fig. S5(a). Representative Wigner tomography snapshots at selected times for initial state $|+\rangle|2\rangle$ are shown in Fig. S5(b). We observe that the CZ gate time is reduced from $\sim 5.5 \mu\text{s}$ to $\sim 2.5 \mu\text{s}$.

It is important to note that the gate time is reduced

by more than a factor of two as the resonant condition is shifted by $n\chi_B$ when the control cavity is prepared in $|n\rangle$ in accordance with Eq. S7. Since the gate detuning is defined with respect to the single-photon case and is kept constant for both experiments, the effective detuning becomes smaller for the two-photon state, leading to a gate rate that exceeds the simple factor-of-two scaling expected from bosonic enhancement alone. This entails that when the engineered dynamics is applied to multiphoton states, we must account for this difference in effective detuning appropriately.

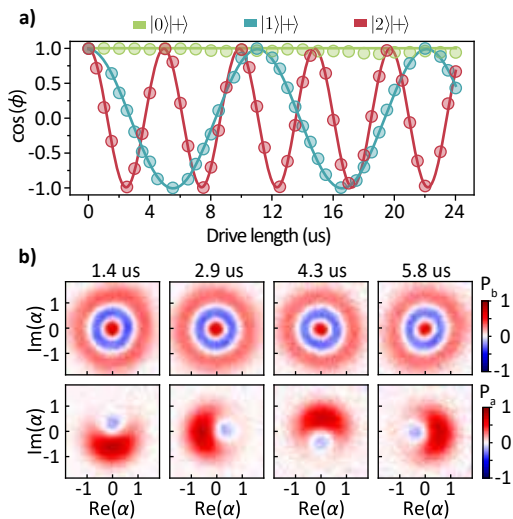


FIG. S5. **Bosonic enhancement of the gate rate.** (a) Phase acquired by the target cavity initialized in $|+\rangle$ during the gate when the control cavity is prepared in $|0\rangle$, $|1\rangle$ and $|2\rangle$. The gate time is reduced from $\sim 5.5\mu\text{s}$ to $\sim 2.5\mu\text{s}$ when populating the control cavity with two photons. (b) Representative Wigner tomography snapshots of the target cavity at selected times for the initial state $|+\rangle|2\rangle$.

S8. PAULI BARS FOR OTHER STATES

Here, we present the Pauli decomposition of the reconstructed two-cavity states after 0 to 6 applied gates for the set of initial states $|+\rangle|0\rangle$, $|1\rangle|+\rangle$ and $|+\rangle|+\rangle$ in Fig. S6. For initial state $|+\rangle|+\rangle$ we further distinguish between the case of drive on and off (i.e. $g_{CZ} = 0$). These data complement Fig. 3 of the main text, where the state fidelity is shown as a function of applied gates.

The density matrices are reconstructed from the measurement data using ORENS and Bayesian inference (S9). The colored bars correspond to the experimentally reconstructed Pauli coefficients. The black outlined bars indicate the ideal values, while the dashed lines show the expected coefficients obtained from numerical simulations. The simulations are performed using the effective Hamiltonian $H_{\text{eff}} = g_{CZ}a^\dagger ab^\dagger b$ with a gate time of $5.5\mu\text{s}$ and including cavity decoherence as the only loss channel with $T_{1A} = 210\mu\text{s}$, $T_{\phi A} = 70\mu\text{s}$, $T_{1B} = 388\mu\text{s}$ and

$$T_{\phi B} = 52\mu\text{s}.$$

Furthermore, we show in Fig. S7 the reconstructed Pauli decompositions after a single gate applied to the initial states $|-\rangle|-\rangle$, $|i\rangle|i\rangle$ and $|-i\rangle|-i\rangle$, which ideally produce maximally entangled states under the engineered interaction.

As above, the Pauli coefficients are obtained from measurements using ORENS combined with Bayesian inference. The experimental results are compared to both the ideal states (black outline) and to numerical simulations including decoherence (dashed lines) using the same effective Hamiltonian and parameters described above.

S9. QUANTUM STATE RECONSTRUCTION

We perform quantum state reconstruction following the Optimized Reconstruction with Excitation Number Sampling (ORENS) protocol. We extended the scheme in Ref. [59] for reconstructing two-mode cavity state. It involves applying a set of optimized displacement points on both cavities and performing photon number measurements. The measurement results are then processed to estimate the two-mode density matrix. Up to this point, the resulting density matrix might not be physical due to the presence of noise in experimental data. We then employ Bayesian inference to get a statistically accurate and physical estimated density matrix.

The following two sections provide details on the implementation of the ORENS protocol and the Bayesian inference procedure used to get the final estimated density matrix.

A. State reconstruction via ORENS

ORENS enables efficient quantum state tomography using the theoretical minimum number of measured single-valued observables, which are excitation (photon) number measurements performed after a set of optimized phase-space displacements. For example, for reconstructing a single bosonic mode of dimension D , the least number of observables can be $N_{\text{obs}} = D^2 - 1$, which are obtained using N_{obs} optimized displacement points and measuring a single photon number n . The set of observables can be written as $X_i = \text{tr}(|n\rangle\langle n|\hat{D}^\dagger(\alpha_i)\rho\hat{D}(\alpha_i))$, where $i = 1, 2, \dots, N_{\text{obs}}$ and $\{\alpha_i\}$ is the set of optimized displacement points obtained by minimizing the measurement matrix via gradient descent algorithm [59].

An arbitrary density matrix ρ of dimension D can be parametrized by its D^2 real parameters (without the normalization condition). In our case, we take the diagonal elements of ρ as well as its real and imaginary off-diagonal (upper triangular) elements, which we shall arrange in a vector form \vec{Y} . The parameters (\vec{Y}) and observables (also arranged in a vector form \vec{X}) are linearly related [69]. In our case, we write this as $\vec{Y} = M\vec{X}$.

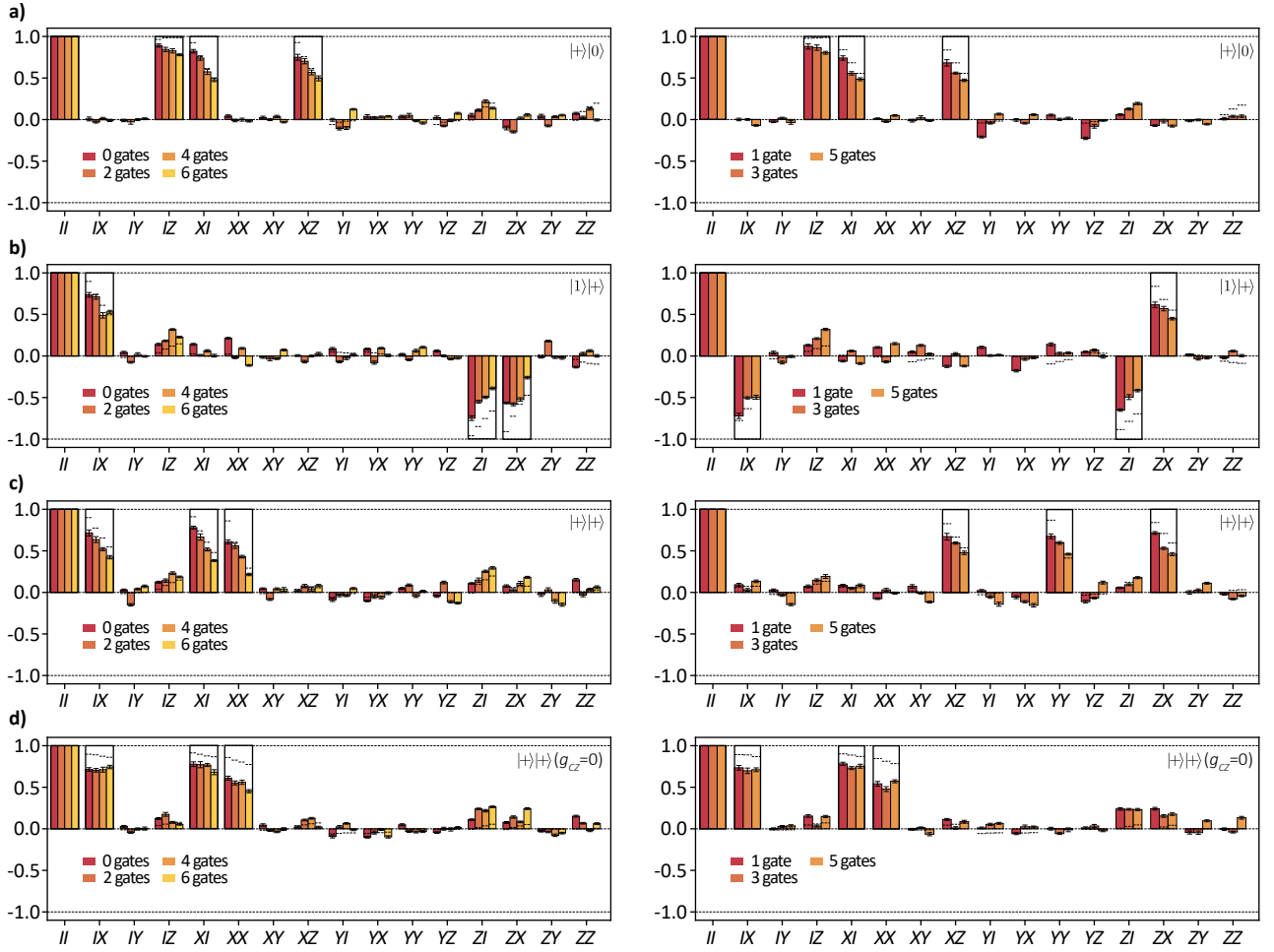


FIG. S6. **Pauli decompositions for repeated gate application.** Reconstructed Pauli bars of the two-cavity states after 0–6 applied gates for the initial states $|+\rangle|0\rangle$ (a), $|1\rangle|+\rangle$ (b), and $|+\rangle|+\rangle$ (with drive on (c) and off (d)). Black outlines indicate the ideal values and dashed lines the numerical simulations including cavity decoherence.

Here, M is a mapping matrix, which can be computed given the set of optimized displacement points $\{\alpha_i\}$ and photon number n to be measured. To get an estimate of the parameters \vec{Y}_{est} , given the experimental data \vec{X} , we apply the inverse of the matrix equation $\vec{Y}_{\text{est}} = M^+ \vec{X}$ with $M^+ = (M^\dagger M)^{-1} M^\dagger$ being the left Moore-Penrose pseudoinverse. From the estimated parameters, we then construct the density matrix ρ_{LS} . Given this density matrix, which might not be physical, we employ Bayesian inference to get the final physical density matrix (see the next section).

Now, to reconstruct a two-mode cavity state in the present case, we use a total dimension of $D = 4$ (2 for each mode) and $D = 9$ (3 for each mode) for the case of 0/1 encoding and 0/2 encoding, respectively. The displacement operations we apply are of the form $\{\hat{D}_A(\alpha_i) \otimes \hat{D}_B(\alpha_j)\}$, where $\{\alpha_i\}$ refers to the optimized displacements obtained via optimization for the single-mode tomography case. For the 0/1 and 0/2 encoding, we have a total of 25 and 100 different displacements, respectively. This exceeds the theoretical minimum of $D^2 - 1$ in both encoding

scenarios. After each displacement, we measure the probability of observing the photon number $|n\rangle_A \otimes |n\rangle_B$ in the two-mode cavity state. This is obtained through individual single-shot measurements of photon number $|n\rangle$ in cavity A and B , which is done by applying a selective π -pulse on the side qubit q_A and q_B tuned at the frequency $\omega_{q_A} - n\chi_{Aq_A}$ and $\omega_{q_B} - n\chi_{Bq_B}$, respectively, and measuring the qubit population in the excited state. By correlating the outcomes of these measurements, we obtain the joint probability of observing $|n\rangle_A \otimes |n\rangle_B$ photons.

Note that as we use parametrization with D^2 parameters (without enforcing the normalization condition), the density matrix obtained via linear inversion (least square) ρ_{LS} might not have unit trace and positive eigenvalues. We shall keep ρ_{LS} as a data-driven estimator that faithfully reflects the measurement outcomes, and use it solely as the reference point for a subsequent Bayesian inference procedure that restores physicality in the final estimated density matrix.

Two-mode state reconstruction has previously been also achieved by measuring the joint parity $\langle \hat{P}_A \otimes$

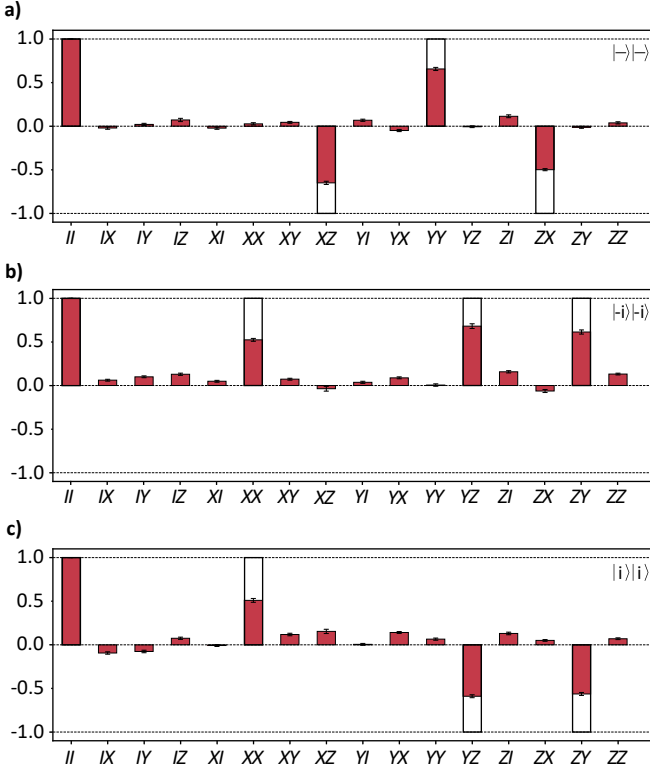


FIG. S7. **Pauli decompositions for maximally entangled states.** Reconstructed Pauli bars after a single gate applied to the initial states $|-\rangle|-\rangle$ (a), $|-i\rangle|-i\rangle$ (b), and $|i\rangle|i\rangle$ (c). Black outlines correspond to ideal states, and dashed lines to numerical simulations including cavity decoherence.

\hat{P}_B) [70]. However, this approach requires closely matched dispersive shifts χ between transmon and both cavities, placing stringent constraints on the hardware. One can in principle perform separated single shot parity measurements for \hat{P}_A and \hat{P}_B , and correlate them to get $\langle \hat{P}_A \otimes \hat{P}_B \rangle$, as we did for photon number in this work. However, the traditional parity measurement $\pi/2$ -wait- $\pi/2$ is known to suffer from coherent as well as incoherent errors [59]. A standard technique employed to counter this is to perform corrected parity, in which $\langle \hat{P} \rangle_{\text{corr}} = (\langle \hat{P} \rangle - \langle \hat{P} \rangle_{\text{rev}})/2$, where $\langle \hat{P} \rangle_{\text{rev}}$ is performed with a $\pi/2$ -wait- $(-\pi/2)$ (different) sequence. Implementing this technique in our device would require correlating 4 different measurements: \hat{P}_A with \hat{P}_B ; \hat{P}_A with $\hat{P}_{B,\text{rev}}$; $\hat{P}_{A,\text{rev}}$ with \hat{P}_B ; and $\hat{P}_{A,\text{rev}}$ with $\hat{P}_{B,\text{rev}}$, therefore multiplying the number of required measurements by a factor of 4. This tomography method will add a factor of 2^N to the total number of displacement points for N -mode state reconstruction, which is certainly less favorable compared to the method implemented in this work.

B. Bayesian Inference

To get a physical (positive semidefinite) estimated density matrix, a standard technique is to perform linear inversion (as explained in the previous section) followed by maximum likelihood [71]. However, this method suffers from the problem, that the estimated physical density matrix often has zero eigenvalues [72]. This means one will never get a given result if the measurement is done in the corresponding basis, which is not justifiable from measurements with finite repetition.

Instead, we employ Bayesian inference, which gives a statistically more accurate estimate. Incorporating Bayes' rule, Bayesian inference gives a posterior probability distribution given the measured experimental data and prior knowledge. The posterior distribution can then be used (sampled) to get an estimate for any function of the density matrix. We follow an efficient Bayesian inference protocol introduced in Ref. [73]. We use uniform prior, i.e., no prior assumption on the density matrix, such that the posterior distribution is proportional to the pseudo likelihood function

$$\mathcal{L}(\rho) \propto \exp\left(-\frac{N}{2}\|\rho - \rho_{LS}\|^2\right) \quad (\text{S22})$$

where $\|\cdot\|$ is the Frobenius norm and N is the total number of events (number of repetitions times number of displacements applied). We then draw a total of RT samples according to the Crank-Nicolson Metropolis-Hastings procedure with a thinning parameter $T = 2^7$ to reduce serial correlation in the subsequent samplings and keep only $R = 2^{10}$ samples.

The final reconstructed state is given by the Bayesian mean estimator:

$$\rho_{\text{BME}} = \frac{1}{R} \sum_{r=1}^R \rho_r \quad (\text{S23})$$

where $\{\rho_r\}$ are the retained physical density matrices sampled from the posterior distribution.

We calculate the fidelity between the density matrix ρ_{BME} and a target density matrix ρ_{tar} using:

$$\mathcal{F} = \left(\text{Tr} \sqrt{\sqrt{\rho_{\text{tar}}} \rho_{\text{BME}} \sqrt{\rho_{\text{tar}}}} \right)^2, \quad (\text{S24})$$

where ρ_{tar} is the target density matrix generated by simulating the numerical GRAPE pulses under realistic decoherence mechanisms followed by propagation through an ideal gate model with no decoherence, where the effective Hamiltonian used is $\hat{H}_{\text{eff}} = g\hat{a}^\dagger \hat{a} \hat{b}^\dagger \hat{b}$. This procedure isolates the sources of gate imperfections, such as system decoherence and spurious coupler excitations, from errors of the state preparation and measurement. A quantitative error budget is provided in Section S11.

S10. DRIVEN INDUCED DECOHERENCE

A. Strong-Drive Effects on Cavity Coherence

In this study, we drive the coupler with a strong microwave tone to activate the cross-Kerr interaction. When operating in the Raman regime, the coupler is never physically populated. This, to first order, circumvents the imperfections caused directly by its decoherence mechanisms. Nevertheless, we observe a substantial reduction of the oscillator decoherences as a function of drive strength and detuning to the resonance condition described in the main text.

To quantify the cavity properties under this strong drive, we characterize the driven single-photon lifetime of the oscillators by loading a photon in Alice (Bob) and replacing the delay time by a strong off-resonant drive applied to the coupler. We observe a degradation of T_1 times from 700–900 μs (800–1000 μs) to ~ 210 μs (~ 390 μs). The dephasing time of the oscillators was characterized via a Ramsey experiment where Alice (Bob) is initialized in a superposition $\frac{|0\rangle+|1\rangle}{\sqrt{2}}$ and the delay time is replaced with a strong off-resonant drive. We observe a reduction in the oscillator T_2^* times from 500–600 μs (700–900 μs) to ~ 40 μs (~ 60 μs).

This substantial reduction is consistent with previous observations [43, 51, 55] in strongly driven cQED systems. We attribute this enhanced decay of the oscillators to the drive-induced decay [51, 67] that results from the dressing of the coupler by the off-resonant coherent exchange interaction. We can model this naively by considering the first-order perturbative correction to the coupler decay operator, $|g\rangle\langle e| \rightarrow |g\rangle\langle e| + [\hat{S}, |g\rangle\langle e|]$, where the SWT generator \hat{S} used in Section S4 results in an extra term $\beta_g ab^\dagger (|g\rangle\langle g| - |e\rangle\langle e|)$. Likewise, the dressing of the coupler dephasing yields $\beta_g (a^\dagger b |g\rangle\langle e| + ab^\dagger |e\rangle\langle g|)$. Since we operate the coupler away from its sweet spot, with dephasing time $T_\phi \sim 2$ μs , the dressed oscillator decay is then given by $\sim \beta_g^{-2} T_\phi \sim 200$ μs . Similar to [51], there is a tradeoff between the gate time that is proportional to Δ and the sideband-dressed oscillator decay that decays as Δ^{-2} . While this simple model yields a qualitatively consistent prediction to our observations, a more rigorous approach is needed to systematically explain such drive-induced decoherence effects. This is an active field of research and outside the immediate scope of this work.

Further, the applied drive induces AC Stark shifts of the ancilla transition frequencies. As the drive amplitude increases, dressed ancilla transitions may move closer to the cavity frequencies, enhancing hybridization and increasing the inherited cavity decay [31].

We attribute the degradation of the oscillator dephasing time to two different causes. First, dressed dephasing [31] due to the elevated ancilla temperature in the Floquet basis. This dephasing is only affected by the drive-coupler detuning (~ 280 MHz), and hence is

insensitive to $\Delta \sim 6$ MHz, producing a flat photon-shot noise [51]. Second, the interplay between the enhanced oscillator decay rates and the direct cross-Kerr coupling between the oscillators inducing a cross-Kerr dependent dephasing.

B. Driven Coupler Decoherence

The decay observed in the coherent exchange experiment — where the populations of Alice, Bob, and the coupler are recorded as a function of drive duration under the interaction $g_{ab} a^\dagger b q + \text{h.c.}$ — cannot be explained using the free-evolution dephasing time extracted from Ramsey measurements. Simulations incorporating the dephasing time T_ϕ extracted from the coupler Ramsey experiments predict a significantly faster decay of the exchange oscillations than is experimentally observed. This discrepancy therefore indicates that the relevant coherence properties during the exchange process differ from those inferred from standard Ramsey measurements.

It is well established that under continuous driving, the effective coherence times of a superconducting qubit or cavity are modified relative to their free-evolution values [74, 75]. Consequently, the coherent exchange dynamics must be described in terms of effective driven decay processes.

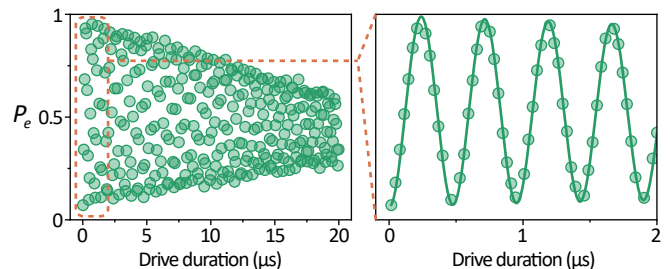


FIG. S8. **Sideband decay.** The measured coherent exchange oscillations of the coupler mode q_C are fitted using Eq. S25 to determine the corresponding decay and dephasing times. The right panel shows a zoomed-in view of the first 2, μs of the oscillations.

We model the dynamics within the subspace $\{|1\rangle|0\rangle|g\rangle, |0\rangle|1\rangle|e\rangle\}$ by including both population leakage and dephasing processes. Here, κ_ϕ denotes the effective dephasing rate within the exchange subspace, while κ_1 characterizes population leakage out of it. To extract both rates, we fit the measured population of the coupler during the coherent exchange interaction to the expression [55]:

$$P_0(t) = Ae^{-\kappa_1 t} \left(1 + e^{-\kappa_\phi t} \cos(2g_1 t + \phi_0) \right) + B \quad (\text{S25})$$

From this fit, we obtain the corresponding effective coherence times of $T_{1\text{eff}} = 94 \pm 3$ μs and $T_{\phi\text{eff}} = 28.0 \pm 0.4$ μs .

We emphasize that these times should not be interpreted as driven coherence times of an individual cir-

cuit element. Rather, they quantify the effective relaxation and dephasing processes of the coupled subspace $\{|1\rangle|0\rangle|g\rangle, |0\rangle|1\rangle|e\rangle\}$ during the coherent exchange interaction.

Furthermore, we also perform a full master equation simulation with the measured coupler dephasing time obtained using a CPMG sequence ($13\ \mu\text{s}$). The resulting dynamics reproduces the experimental data, as shown in Fig. 2 of the main text. We can understand this by noting that under the drive, the qubit Bloch sphere constantly rotates and the subsequent dynamics resembles that under a repeated echo sequence.

S11. ERROR BUDGETING

In this section we estimate the sources of infidelity using master equation simulations and compare them to the experimentally measured values. We isolate each error mechanism by introducing them one at a time in the simulation. This provides a gauge of the individual contributions but does not account for the potential correlations between them. Thus, we also provide the analysis where all errors are included in a single simulation as a comparison. Overall, both of these approaches offer a fairly consistent reproduction of the experimental results.

To illustrate, we analyze the state after the application of a single CZ gate for a set of initial states introduced in the main text. Our gate is modeled in simulation by the effective Hamiltonian

$$H_{eff} = g_{CZ} a^\dagger a b^\dagger b + \chi_A a^\dagger a q^\dagger q + \chi_B b^\dagger b q^\dagger q \quad (\text{S26})$$

As a first source of infidelity, we consider errors due to state preparation and measurement (SPAM). In the ideal scenario, we simulate the numerical pulses used to create our initial states without decoherence and subsequently apply an ideal CZ gate. We simulate ORENS measurement using a pulse-based approach, where the duration of the selective π -pulse (gaussian pulse shape) as well as displacement pulse (constant pulse shape with cosine square on and off ramp) from experiments are taken into account.

In the ideal case, we neglect decoherence during the ORENS protocol as well as readout errors. The infidelity of the final simulated reconstructed state is evaluated as $1 - |\langle \psi_{\text{sim}} | \psi_{\text{target}} \rangle|^2$, where ψ_{target} refers to the expected state after application of one gate (e.g. $|1\rangle|-\rangle$ for initial state $|1\rangle|+\rangle$). The resulting infidelity is shown as the turquoise bar in Fig. S9.

We repeat the previous analysis, but now include decoherence during initial state creation and ORENS as well as measurement error. The infidelity is shown as the red bar in Fig. S9. During the tomography process, we measure the correlated excited state population of the side auxiliary transmons, which amounts to evaluating the expectation value $q_A^\dagger q_A \otimes q_B^\dagger q_B$ in simulation. We include measurement error by evaluating

$$R_A \otimes R_B, \quad (\text{S27})$$

with

$$R_i = P_i(e|e)q_i^\dagger q_i + P_i(e|g)(q_i^\dagger q_i - \mathbb{I}), \quad (\text{S28})$$

where $P_i(e|e/g)$ refers to the probability of measuring $|e\rangle$ given $|e\rangle/|g\rangle$, which reflects the experimentally measured readout errors.

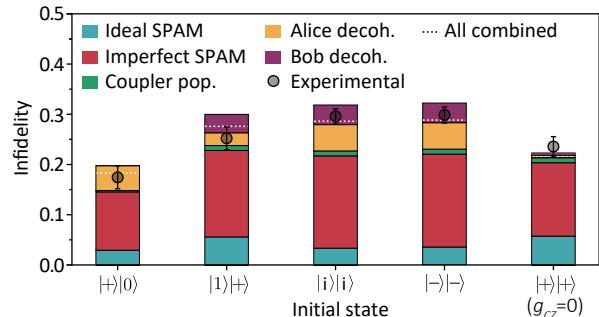


FIG. S9. **Simulated error budget for a single CZ gate.** Stacked bars show simulated contributions to the infidelity from SPAM, coupler population, and cavity decoherence for several initial states. Black markers indicate experimentally measured infidelities.

In subsequent steps we consider additional error mechanisms, including residual coupler population (green) and decoherence of Alice (gold) and Bob (purple) during the gate time. For these simulations we use the experimentally measured driven coherence times of all system elements. Each contribution to the remaining error budget in Fig. S9 is simulated by only including one error mechanism at a time and not considering SPAM errors.

Overall, for a single gate, the SPAM errors dominate the infidelity, whereas for increasing numbers of gates cavity decoherence becomes the leading error mechanism (shown in the main text). While the overall trend of infidelity over several gates is in good agreement with experimental data, we note that for some individual points simulation predicts worse results than experiment. In simulations, a significant portion of the infidelity during the ORENS protocol arises from a small amount of leakage outside the 0/1 subspace, which cannot be captured using ORENS state reconstruction with $D=2$. However, experimentally we did not observe higher cavity populations after the gate. This is likely due to the effects of decoherence, which is independently considered in this simple model but affects the dynamics in conjunction with the imperfect state preparation in the experiment.

S12. PROTOCOL USING 3 WAVE MIXING COUPLER

Our Raman-assisted protocol to engineer cross-Kerr using a SQUID coupler consists on concatenating two 4-wave mixing Hamiltonian components to create an effective 6-wave mixing term. While this process is effective in activating the desired cross-Kerr dynamics, it does

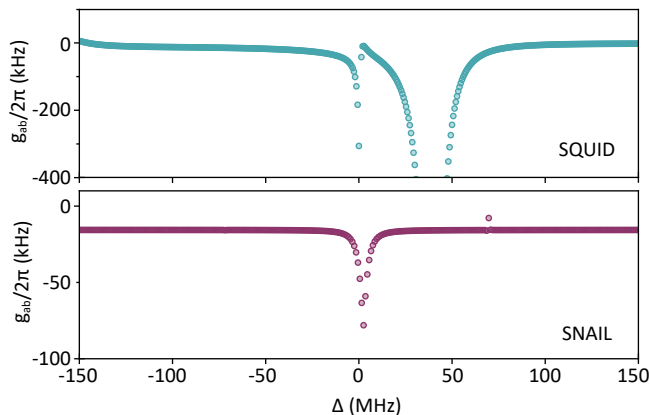


FIG. S10. **Cross-Kerr protocol adapted to SNAIL.** Top: Cross-Kerr predicted with Floquet simulations using the SQUID coupler considered in the main text. Bottom: Cross-Kerr using a SNAIL coupler. The only dominant transition is the one considered in Eq. S29.

come with a few inconvenient parasitic terms. Notably, the most problematic ones are the always-on dispersive shifts between the cavities and the coupler, which change the effective detuning of the drive from the coherent exchange condition as a function of photon number population in the cavities. Furthermore, the AC Stark shift stemming from the four-wave-mixing dynamics also complicates the spectral landscape and could cause undesired frequency collisions under strong drives.

To mitigate these imperfections that stem from the 4-wave-mixing process, we can consider a tailored 3-wave mixing element instead. For instance, a linear inductive coupler (LINC) [76] or a SNAIL biased to the operating point where it only exhibits 3- and 5-wave mixing [52]. For the remainder of this section we focus on the SNAIL

as a concrete example.

Driving at

$$\omega_d^{(3)} = \omega_c - \omega_a \quad (\text{S29})$$

engineers the dynamics given by

$$\hat{H}_d^{(3)}/\hbar = g^{(3)} \left(\hat{a}^\dagger |g\rangle \langle e| + \hat{a} |e\rangle \langle g| \right), \quad (\text{S30})$$

and

$$\hat{H}_d^{(5)}/\hbar = g^{(5)} \left(\hat{a}^\dagger \hat{b}^\dagger \hat{b} |g\rangle \langle e| + \hat{a} \hat{b} \hat{b}^\dagger |e\rangle \langle g| \right), \quad (\text{S31})$$

since both are resonant at the same condition, with interaction rates given by $g^{(3)} = c^{(3)}\phi_c^2\phi_a$ and $g^{(5)} = c^{(5)}\phi_c^2\phi_a\phi_b^2$. Here, $c^{(3)}$ and $c^{(5)}$ are coefficients that depend on the operating point [52].

Similar to the SQUID case, driving the system with a detuning Δ from this condition leads, within the second-order RWA, to the effective interaction

$$\hat{H}_{\text{eff}}^{(3)}/\hbar = \frac{g^{(3)}g^{(5)}}{\Delta} \hat{a}^\dagger \hat{a} \hat{b}^\dagger \hat{b} |g\rangle \langle g|. \quad (\text{S32})$$

Here we have considered that the drive is long and weak enough to avoid leakage to higher energy levels of the SNAIL coupler, effectively treating it as a two-level system.

The main advantage of this approach is the suppression of multi-photon processes that comes from using a 3-wave mixing element, compared to the SQUID coupler. We used the Floquet simulations explained in Section S5 to predict the cross-Kerr between two oscillators coupled through a SNAIL element, which results in a cleaner spectrum, with fewer spurious transitions compared to the SQUID case, see Fig. S10.

-
- [1] C. H. Bennett and G. Brassard, Quantum cryptography: Public key distribution and coin tossing, *Theoretical computer science* **560**, 7 (2014).
 - [2] N. Gisin, G. Ribordy, W. Tittel, and H. Zbinden, Quantum cryptography, *Reviews of modern physics* **74**, 145 (2002).
 - [3] S. Pirandola, U. L. Andersen, L. Banchi, M. Berta, D. Bunandar, R. Colbeck, D. Englund, T. Gehring, C. Lupo, C. Ottaviani, *et al.*, *Advances in quantum cryptography*, *Advances in optics and photonics* **12**, 1012 (2020).
 - [4] H. J. Kimble, The quantum internet, *Nature* **453**, 1023 (2008).
 - [5] S. Wehner, D. Elkouss, and R. Hanson, Quantum internet: A vision for the road ahead, *Science* **362**, eaam9288 (2018).
 - [6] N. Ofek, A. Petrenko, R. Heeres, P. Reinhold, Z. Leghtas, B. Vlastakis, Y. Liu, L. Frunzio, S. M. Girvin, L. Jiang, *et al.*, Extending the lifetime of a quantum bit with error correction in superconducting circuits, *Nature* **536**, 441 (2016).
 - [7] V. V. Sivak, A. Eickbusch, B. Royer, S. Singh, I. Tsioutsios, S. Ganjam, A. Miano, B. L. Brock, A. Z. Ding, L. Frunzio, *et al.*, Real-time quantum error correction beyond break-even, *Nature* **616**, 50 (2023).
 - [8] Z. Ni, S. Li, X. Deng, Y. Cai, L. Zhang, W. Wang, Z.-B. Yang, H. Yu, F. Yan, S. Liu, *et al.*, Beating the break-even point with a discrete-variable-encoded logical qubit, *Nature* **616**, 56 (2023).
 - [9] S. Shirol, S. van Geldern, H. Xi, and C. Wang, Passive quantum error correction of photon loss at breakeven, arXiv preprint arXiv:2510.19794 (2025).
 - [10] C. Flühmann, T. L. Nguyen, M. Marinelli, V. Negnevitsky, K. Mehta, and J. P. Home, Encoding a qubit in a trapped-ion mechanical oscillator, *Nature* **566**, 513 (2019).
 - [11] B. De Neeve, T.-L. Nguyen, T. Behrle, and J. P. Home, Error correction of a logical grid state qubit by dissipative pumping, *Nature Physics* **18**, 296 (2022).
 - [12] M. V. Larsen, J. E. Bourassa, S. Kocsis, J. F. Tasker,

- R. S. Chadwick, C. González-Arciniegas, J. Hastrup, C. E. Lopetegui-González, F. M. Miatto, A. Motamedi, *et al.*, Integrated photonic source of Gottesman–Kitaev–Preskill qubits, *Nature* **642**, 587 (2025).
- [13] S. Konno, W. Asavanant, F. Hanamura, H. Nagayoshi, K. Fukui, A. Sakaguchi, R. Ide, F. China, M. Yabuno, S. Miki, *et al.*, Logical states for fault-tolerant quantum computation with propagating light, *Science* **383**, 289 (2024).
- [14] A. Furusawa, J. L. Sørensen, S. L. Braunstein, C. A. Fuchs, H. J. Kimble, and E. S. Polzik, Unconditional quantum teleportation, *science* **282**, 706 (1998).
- [15] S.-K. Liao, W.-Q. Cai, W.-Y. Liu, L. Zhang, Y. Li, J.-G. Ren, J. Yin, Q. Shen, Y. Cao, Z.-P. Li, *et al.*, Satellite-to-ground quantum key distribution, *Nature* **549**, 43 (2017).
- [16] S. Konno, W. Asavanant, F. Hanamura, H. Nagayoshi, K. Fukui, A. Sakaguchi, R. Ide, F. China, M. Yabuno, S. Miki, *et al.*, Propagating Gottesman–Kitaev–Preskill states encoded in an optical oscillator, arXiv preprint arXiv:2309.02306 (2023).
- [17] M. Tse, H. Yu, N. Kijbunchoo, A. Fernandez-Galiana, P. Dupej, L. Barsotti, C. Blair, D. Brown, S. e. Dwyer, A. Effler, *et al.*, Quantum-enhanced advanced LIGO detectors in the era of gravitational-wave astronomy, *Physical Review Letters* **123**, 231107 (2019).
- [18] W. Jia, V. Xu, K. Kuns, M. Nakano, L. Barsotti, M. Evans, N. Mavalvala, L. S. Collaboration†, R. Abbott, I. Abouelfettouh, *et al.*, Squeezing the quantum noise of a gravitational-wave detector below the standard quantum limit, *Science* **385**, 1318 (2024).
- [19] H.-S. Zhong, H. Wang, Y.-H. Deng, M.-C. Chen, L.-C. Peng, Y.-H. Luo, J. Qin, D. Wu, X. Ding, Y. Hu, *et al.*, Quantum computational advantage using photons, *Science* **370**, 1460 (2020).
- [20] L. S. Madsen, F. Laudenbach, M. F. Askarani, F. Rortais, T. Vincent, J. F. Bulmer, F. M. Miatto, L. Neuhaus, L. G. Helt, M. J. Collins, *et al.*, Quantum computational advantage with a programmable photonic processor, *Nature* **606**, 75 (2022).
- [21] D. E. Chang, V. Vuletić, and M. D. Lukin, Quantum nonlinear optics—photon by photon, *Nature Photonics* **8**, 685 (2014).
- [22] I. L. Chuang and Y. Yamamoto, Simple quantum computer, *Physical Review A* **52**, 3489 (1995).
- [23] M. Paternostro, M. Kim, and B. Ham, Generation of entangled coherent states via cross-phase-modulation in a double electromagnetically induced transparency regime, *Physical Review A* **67**, 023811 (2003).
- [24] S. Ding, G. Maslennikov, R. Hablützel, and D. Matuskevich, Cross-kerr nonlinearity for phonon counting, *Physical review letters* **119**, 193602 (2017).
- [25] W. Chen, J. Gan, J.-N. Zhang, D. Matuskevich, and K. Kim, Quantum computation and simulation with vibrational modes of trapped ions, *Chinese Physics B* **30**, 060311 (2021).
- [26] S. Rosenblum, Y. Y. Gao, P. Reinhold, C. Wang, C. J. Axline, L. Frunzio, S. M. Girvin, L. Jiang, M. Mirrahimi, M. H. Devoret, *et al.*, A cnot gate between multiphoton qubits encoded in two cavities, *Nature communications* **9**, 652 (2018).
- [27] Y. Y. Gao, B. J. Lester, K. S. Chou, L. Frunzio, M. H. Devoret, L. Jiang, S. Girvin, and R. J. Schoelkopf, Entanglement of bosonic modes through an engineered exchange interaction, *Nature* **566**, 509 (2019).
- [28] Y. Xu, Y. Ma, W. Cai, X. Mu, W. Dai, W. Wang, L. Hu, X. Li, J. Han, H. Wang, *et al.*, Demonstration of controlled-phase gates between two error-correctable photonic qubits, *Physical review letters* **124**, 120501 (2020).
- [29] K. Reuer, J.-C. Besse, L. Wernli, P. Magnard, P. Kurpiers, G. J. Norris, A. Wallraff, and C. Eichler, Realization of a universal quantum gate set for itinerant microwave photons, *Physical Review X* **12**, 011008 (2022).
- [30] Y. Y. Gao, B. J. Lester, Y. Zhang, C. Wang, S. Rosenblum, L. Frunzio, L. Jiang, S. Girvin, and R. J. Schoelkopf, Programmable interference between two microwave quantum memories, *Physical Review X* **8**, 021073 (2018).
- [31] Y. Zhang, B. J. Lester, Y. Y. Gao, L. Jiang, R. Schoelkopf, and S. Girvin, Engineering bilinear mode coupling in circuit QED: Theory and experiment, *Physical Review A* **99**, 012314 (2019).
- [32] U. Goldblatt, N. Kahn, S. Hazanov, O. Milul, B. Guttel, L. M. Joshi, D. Chaousovsky, F. Lafont, and S. Rosenblum, Recovering quantum coherence of a cavity qubit coupled to a noisy ancilla through real-time feedback, *Physical Review X* **14**, 041056 (2024).
- [33] K. Sahay, J. Jin, J. Claes, J. D. Thompson, and S. Puri, High-threshold codes for neutral-atom qubits with biased erasure errors, *Physical Review X* **13**, 041013 (2023).
- [34] J. Mai, Q. Liu, X. Deng, Y. Cai, Z. Ni, L. Zhang, L. Hu, P. Zheng, S. Liu, Y. Xu, *et al.*, A biased-erasure cavity qubit with hardware-efficient quantum error detection, arXiv preprint arXiv:2601.21616 (2026).
- [35] S. Qin and H. K. Ng, Crot gate (2026), manuscript in preparation.
- [36] J. Zimmerman, Sensitivity enhancement of superconducting quantum interference devices through the use of fractional-turn loops, *Journal of Applied Physics* **42**, 4483 (1971).
- [37] B. J. Chapman, S. J. De Graaf, S. H. Xue, Y. Zhang, J. Teoh, J. C. Curtis, T. Tsunoda, A. Eickbusch, A. P. Read, A. Koottandavida, *et al.*, High-on-off-ratio beam-splitter interaction for gates on bosonically encoded qubits, *PRX Quantum* **4**, 020355 (2023).
- [38] J. R. Schrieffer and P. A. Wolff, Relation between the Anderson and Kondo Hamiltonians, *Physical Review* **149**, 491 (1966).
- [39] A. Copetudo, A. M. Kasper, T. Krisnanda, G. Veyrac, S. Qin, H. K. Ng, and Y. Y. Gao, Supplementary information: A direct controlled-phase gate between microwave photons.
- [40] A. L. Grimsmo, J. Combes, and B. Q. Baragiola, Quantum computing with rotation-symmetric bosonic codes, *Physical Review X* **10**, 011058 (2020).
- [41] J. D. Teoh, P. Winkel, H. K. Babla, B. J. Chapman, J. Claes, S. J. de Graaf, J. W. Garmon, W. D. Kalfus, Y. Lu, A. Maiti, *et al.*, Dual-rail encoding with superconducting cavities, *Proceedings of the National Academy of Sciences* **120**, e2221736120 (2023).
- [42] K. S. Chou, T. Shemma, H. McCarrick, T.-C. Chien, J. D. Teoh, P. Winkel, A. Anderson, J. Chen, J. C. Curtis, S. J. de Graaf, *et al.*, A superconducting dual-rail cavity qubit with erasure-detected logical measurements, *Nature Physics* **20**, 1454 (2024).
- [43] L. Carde, P. Rouchon, J. Cohen, and A. Petrescu, Flux-pump-induced degradation of T₁ for dissipative cat

- qubits, *Physical Review Applied* **23**, 024073 (2025).
- [44] M. Boissonneault, J. M. Gambetta, and A. Blais, Dispersive regime of circuit qed: Photon-dependent qubit dephasing and relaxation rates, *Physical Review A—Atomic, Molecular, and Optical Physics* **79**, 013819 (2009).
- [45] W. Dai, S. Hazra, D. Weiss, P. Kurilovich, T. Connolly, H. Babla, S. Singh, V. Joshi, A. Ding, P. Parakh, *et al.*, Characterization of drive-induced unwanted state transitions in superconducting circuits, *Physical Review X* **16**, 011011 (2026).
- [46] M. Boissonneault, J. M. Gambetta, and A. Blais, Non-linear dispersive regime of cavity qed: The dressed dephasing model, *Physical Review A—Atomic, Molecular, and Optical Physics* **77**, 060305 (2008).
- [47] J. Gambetta, A. Blais, D. I. Schuster, A. Wallraff, L. Frunzio, J. Majer, M. H. Devoret, S. M. Girvin, and R. J. Schoelkopf, Qubit-photon interactions in a cavity: Measurement-induced dephasing and number splitting, *Physical Review A—Atomic, Molecular, and Optical Physics* **74**, 042318 (2006).
- [48] R. W. Heeres, B. Vlastakis, E. Holland, S. Krastanov, V. V. Albert, L. Frunzio, L. Jiang, and R. J. Schoelkopf, Cavity state manipulation using photon-number selective phase gates, *Physical review letters* **115**, 137002 (2015).
- [49] S. Rosenblum, P. Reinhold, M. Mirrahimi, L. Jiang, L. Frunzio, and R. J. Schoelkopf, Fault-tolerant detection of a quantum error, *Science* **361**, 266 (2018).
- [50] P. Reinhold, S. Rosenblum, W.-L. Ma, L. Frunzio, L. Jiang, and R. J. Schoelkopf, Error-corrected gates on an encoded qubit, *Nature Physics* **16**, 822 (2020).
- [51] T. Kim, T. Roy, X. You, A. C. Li, H. Lamm, O. Pronitchev, M. Bal, S. Garattoni, F. Crisa, D. Bafia, *et al.*, Ultracoherent superconducting cavity-based multi-qubit platform with error-resilient control, arXiv preprint arXiv:2506.03286 (2025).
- [52] N. Frattini, U. Vool, S. Shankar, A. Narla, K. Sliwa, and M. Devoret, 3-wave mixing josephson dipole element, *Applied Physics Letters* **110** (2017).
- [53] F. Valadares, A. Dorogov, T. Krisnanda, M. C. Loke, N.-N. Huang, P. Song, and Y. Y. Gao, Flux-activated resonant control of a bosonic quantum memory (2026), arXiv:2602.18122 [quant-ph].
- [54] R. Lescanne, M. Villiers, T. Peronin, A. Sarlette, M. Delbecq, B. Huard, T. Kontos, M. Mirrahimi, and Z. Leghtas, Exponential suppression of bit-flips in a qubit encoded in an oscillator, *Nature Physics* **16**, 509 (2020).
- [55] Y. Lu, A. Maiti, J. W. Garmon, S. Ganjam, Y. Zhang, J. Claes, L. Frunzio, S. M. Girvin, and R. J. Schoelkopf, High-fidelity parametric beamsplitting with a parity-protected converter, *Nature Communications* **14**, 5767 (2023).
- [56] A. Maiti, J. Garmon, Y. Lu, A. Miano, L. Frunzio, and R. Schoelkopf, A linear quantum coupler for clean bosonic control (2025), arXiv preprint arXiv:2501.18025.
- [57] Z. K. Mineev, Z. Leghtas, S. O. Mundhada, L. Christakis, I. M. Pop, and M. H. Devoret, Energy-participation quantization of josephson circuits, *npj Quantum Information* **7**, 131 (2021).
- [58] R. W. Heeres, P. Reinhold, N. Ofek, L. Frunzio, L. Jiang, M. H. Devoret, and R. J. Schoelkopf, Implementing a universal gate set on a logical qubit encoded in an oscillator, *Nature communications* **8**, 94 (2017).
- [59] T. Krisnanda, C. Y. Fontaine, A. Copetudo, P. Song, K. X. Lee, N.-N. Huang, F. Valadares, T. C. Liew, and Y. Y. Gao, Demonstrating efficient and robust bosonic state reconstruction via optimized excitation counting, *PRX Quantum* **6**, 010303 (2025).
- [60] M. Hutchings, J. B. Hertzberg, Y. Liu, N. T. Bronn, G. A. Keefe, M. Brink, J. M. Chow, and B. Plourde, Tunable superconducting qubits with flux-independent coherence, *Physical Review Applied* **8**, 044003 (2017).
- [61] F. Valadares, N.-N. Huang, K. T. N. Chu, A. Dorogov, W. Chua, L. Kong, P. Song, and Y. Y. Gao, On-demand transposition across light-matter interaction regimes in bosonic cqcd, *Nature Communications* **15**, 5816 (2024).
- [62] Y. Sunada, S. Kono, J. Ilves, S. Tamate, T. Sugiyama, Y. Tabuchi, and Y. Nakamura, Fast readout and reset of a superconducting qubit coupled to a resonator with an intrinsic purcell filter, *Physical Review Applied* **17**, 044016 (2022).
- [63] D. T. McClure, H. Paik, L. S. Bishop, M. Steffen, J. M. Chow, and J. M. Gambetta, Rapid driven reset of a qubit readout resonator, *Physical Review Applied* **5**, 011001 (2016).
- [64] J. Koch, T. M. Yu, J. Gambetta, A. A. Houck, D. I. Schuster, J. Majer, A. Blais, M. H. Devoret, S. M. Girvin, and R. J. Schoelkopf, Charge-insensitive qubit design derived from the cooper pair box, *Physical Review A—Atomic, Molecular, and Optical Physics* **76**, 042319 (2007).
- [65] S. O. Mundhada, A. Grimm, S. Touzard, U. Vool, S. Shankar, M. H. Devoret, and M. Mirrahimi, Generating higher-order quantum dissipation from lower-order parametric processes, *Quantum Science and Technology* **2**, 024005 (2017).
- [66] M. Grifoni and P. Hänggi, Driven quantum tunneling, *Physics Reports* **304**, 229 (1998).
- [67] X. You, A. C. Li, T. Roy, S. Zhu, A. Romanenko, A. Grassellino, Y. Lu, and S. Chakram, Floquet-engineered fast snap gates in weakly coupled circuit-qed systems, *Physical Review Applied* **24**, 034072 (2025).
- [68] N. Lambert, E. Giguère, P. Menczel, B. Li, P. Hopf, G. Suárez, M. Gali, J. Lishman, R. Gadhvi, R. Agarwal, *et al.*, Qutip 5: The quantum toolbox in python, *Physics Reports* **1153**, 1 (2026).
- [69] T. Krisnanda, H. Xu, S. Ghosh, and T. C. Liew, Tomographic completeness and robustness of quantum reservoir networks, *Physical Review A* **107**, 042402 (2023).
- [70] C. Wang, Y. Y. Gao, P. Reinhold, R. W. Heeres, N. Ofek, K. Chou, C. Axline, M. Reagor, J. Blumoff, K. Sliwa, *et al.*, A schrödinger cat living in two boxes, *Science* **352**, 1087 (2016).
- [71] J. A. Smolin, J. M. Gambetta, and G. Smith, Efficient method for computing the maximum-likelihood quantum state from measurements with additive gaussian noise, *Physical review letters* **108**, 070502 (2012).
- [72] R. Blume-Kohout, Optimal, reliable estimation of quantum states, *New Journal of Physics* **12**, 043034 (2010).
- [73] J. M. Lukens, K. J. Law, A. Jasra, and P. Lougovski, A practical and efficient approach for bayesian quantum state estimation, *New Journal of Physics* **22**, 063038 (2020).
- [74] F. Yan, S. Gustavsson, J. Bylander, X. Jin, F. Yoshihara, D. G. Cory, Y. Nakamura, T. P. Orlando, and W. D. Oliver, Rotating-frame relaxation as a noise spectrum analyser of a superconducting qubit undergoing driven evolution, *Nature communications* **4**, 2337 (2013).

- [75] G. Ithier, E. Collin, P. Joyez, P. Meeson, D. Vion, D. Esteve, F. Chiarello, A. Shnirman, Y. Makhlin, J. Schrieffer, and G. Schön, Decoherence in a superconducting quantum bit circuit, *Physical Review B* **72**, 134519 (2005).
- [76] A. Maiti, J. W. Garmon, Y. Lu, A. Miano, L. Frunzio, and R. J. Schoelkopf, Linear quantum coupler for clean bosonic control, *PRX Quantum* **6**, 040326 (2025).